



Damage mechanisms of amorphous and low semi-crystalline polymers under tensile deformation studied by Ultra Small Angles X-ray Scattering

Stéphanie Djukic, Anthony Bocahut, Jérôme Bikard, Didier R Long

► To cite this version:

Stéphanie Djukic, Anthony Bocahut, Jérôme Bikard, Didier R Long. Damage mechanisms of amorphous and low semi-crystalline polymers under tensile deformation studied by Ultra Small Angles X-ray Scattering. *Macromolecules*, 2020, 53 (13), pp.5538-5559. 10.1021/acs.macromol.0c00534 . hal-03061218v2

HAL Id: hal-03061218

<https://hal.science/hal-03061218v2>

Submitted on 5 Jan 2021

HAL is a multi-disciplinary open access archive for the deposit and dissemination of scientific research documents, whether they are published or not. The documents may come from teaching and research institutions in France or abroad, or from public or private research centers.

L'archive ouverte pluridisciplinaire **HAL**, est destinée au dépôt et à la diffusion de documents scientifiques de niveau recherche, publiés ou non, émanant des établissements d'enseignement et de recherche français ou étrangers, des laboratoires publics ou privés.

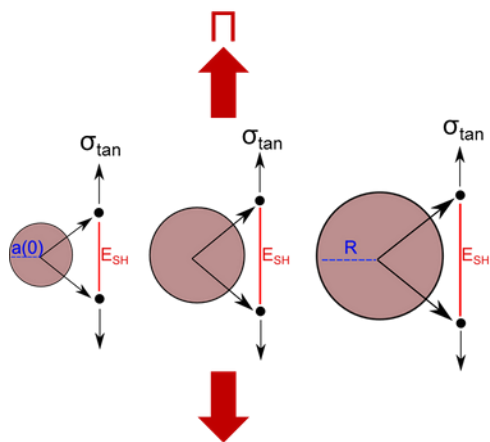
Damage mechanisms of amorphous and low semi-crystalline polymers under tensile deformation studied by Ultra Small Angles X-ray Scattering.

Stéphanie Djukic¹, Anthony Bocahut^{2a}, Jérôme Bikard², Didier R. Long^{1*}

¹ LPMA, Laboratoire des polymères et Matériaux Avancés, UMR 5268 Solvay/CNRS, Solvay in Axel'One, 87 avenue des Frères Perret CS 70061 69192 Cedex, France

² Solvay Research and Innovation Center, 87 avenue des Frères Perret 69192 St-Fons Cedex, France

* Corresponding author. E-mail address: didier.r.long@gmail.com



For Table of Contents use only – Stéphanie Djukic, Anthony Bocahut, Jérôme Bikard, Didier R. Long

Abstract

We investigate the damage mechanisms of amorphous and low semi-crystalline semi-aromatic polyamides, polyphthalamides (PPA) and two other amorphous polymers, polycarbonate (PC) and poly(methyl)methacrylate (PMMA) under tensile deformation. Ultra-Small Angles X-ray Scattering (USAXS) experiments permit to describe the beginning of the damage and the growth of crazes. Interpreting the results allows to measure the volume fractions of damages, as well as their distribution of sizes at different stages of tensile deformation. Different modes of damage are observed. They are initiated by the nucleation of nanometric crazes around pre-existing defects for PC, PMMA and the

^a Present address: Solvay Specialty Polymers, Viale Lombardia 20 20021 Bollate, Italy

amorphous polyamide. Then the growth of these crazes is blocked by the strain hardening at the local level. By increasing the strain further, the growth of a second family of large crazes is observed for these three polymers before the yielding which leads to fracture for PC and PMMA far in the macroscopic strain hardening regime, but not for the amorphous polyamide for which damaged is stabilized after the stress softening and in the ensuing necking regime for which strain hardening is also observed. In the case of two low semi-crystalline polyamides, no damage is observed at all and deformation takes place by necking without damaging and breaking. We propose interpretations for these different behaviors.

Keywords: Polyamides, Crazing, Necking, Strain hardening, USAXS

1 Introduction

Polyamides are engineering thermoplastics which are useful for their mechanical and high barrier properties. They are widely used in textile and automotive industries, where they compete with metals in a context of weight's reduction¹⁻³. Polyamides are generally aliphatic and semi-crystalline such as PA 6, PA 66 or PA 6,10. However, other structures have been developed in the last years for specific applications such as semi-aromatic or aromatic polyamides (MXDA, PA 6T/X, PA 10T/X, PA 10T⁴), as well as amorphous polyamides¹, especially in order to improve the mechanical and thermal properties⁵. Polyphthalamides (PPA) are polyamides containing aromatic rings in their backbones, giving them high mechanical strength and thermal resistance. The resulting PPA may be amorphous or semi-crystalline depending on the combination of monomers used¹. Semi-crystalline PPA are mainly based on PA6T (poly(hexamethylene terephthalamide)), whereas amorphous PPA are mainly based on PA6I (poly(hexamethylene isophthalamide)). These polyamides are generally characterized by higher melting temperatures, higher glass transition temperatures, better chemical resistance, lower moisture absorption and better thermal stability compared to common aliphatic polyamides such as PA 6 and PA 66⁶. These

new PPA are used in several industries such as electronic devices, packaging or automotive industries, in composites for high temperature applications.

Mechanical properties are keys for these applications. The ductile behavior of polymers is controlled by the strain hardening⁷. Strain hardening corresponds to an increase of the stress with deformation in the plastic regime, after the stress softening regime which follows the yield stress. Though its microscopic origin is still under debate⁸⁻²⁰, it is interpreted as a result of a stress contribution of the orienting molecular network^{7,8,21-23}. Strain hardening is a phenomenon observed in the case of amorphous polymers such as Polycarbonate (PC), poly(methyl)methacrylate (PMMA), polyvinyl chloride (PVC), and cellulose diacetate (CDA)²⁴⁻²⁷. Strain hardening can be characterized by the slope of the stress versus strain at large deformations (strain hardening modulus E_{SH})^{9-12,25,28}. Polymers with no or low strain hardening have a fragile behavior characterized by rupture at small deformation, while polymers with a high strain hardening such as polycarbonate²⁹ exhibit better mechanical properties, display a ductile deformation behavior and break –if they do- at large deformation amplitudes. This ductile behavior associated to strain hardening has been explained by Govaert and Meijer²⁸ by the fact that strain hardening prevents strain localization and thus suppresses defects propagation or the appearance of shear bands. As mentioned, even polymers which display strain hardening may eventually break. The issue is: what are the corresponding damage mechanisms? How do they appear? What is the more precise role of strain hardening for stabilizing these damages?

Damaging in polymers under strain has been the subject of research for many years³⁰⁻³⁸. Michler³⁰ has shown that polymers with a 'brittle' behavior such as polystyrene (PS) deform by crazing, whereas polymers considered as 'ductile' deform by shear banding or by homogeneous deformation bands^{31,32,34}. These homogeneous deformation bands are craze-like zones, filled with the stretched polymer. This is the case of polycarbonate (PC). The crazing process takes place in three stages: initiation step, growth and rupture, and is an active research field^{36,38,39}. For describing the growth of crazes, Argon and Salama⁴⁰

introduced in the context of polymers the concept of ‘meniscus-instability model’^{36,38,41}. This hydrodynamic instability had been described by Taylor⁴². In this model, the plastic deformation is initiated by a local effect of stress concentration around the defect, as suggested by Monnerie et al.⁴³. Indeed, the local stress concentration generates a plastic deformation in a thin polymer layer which is surrounded by glassy polymer because this thin polymer layer has not reached its yield point yet. Recently, Michler³⁴ supposed that the initiation of a craze is preceded by the formation of a localized plastic deformation zone. As this plastic deformation zone develops, the hydrostatic stress increases until it becomes higher than a critical stress level. Cavitation can occur, leading to the local development of microvoids. According to Michler³⁴, this localized plastic deformation zone is related to the entanglement network. The second step of the crazing process, the craze growth, is described in literature by a two-step process: the craze tip propagation (‘meniscus-instability model’) and the craze opening, related to the chain entanglements^{38,41,43}. Failure in polymers is assimilated to this last process (craze opening). Recently, experimental studies concerning deformation mechanisms in amorphous polymers and in particular the crazes morphology, generated during tensile experiments, have been done^{44–48}. These studies are performed after the failure of the samples by microscopy (optical microscopy or transmission electron microscopy (TEM)) or X-ray scattering (ultra-small angle X-ray scattering USAXS/SAXS)^{44–47}. Damage during the strain hardening regime has not been studied with the aim of clarifying its role in the stabilizing mechanism of damaged as described macroscopically by Govaert and Meijer²⁸. Most of these studies have also been performed during the last stages of damaged and not at the very beginning of damaging.

Stoclet et al.⁴⁸ performed in-situ USAXS analysis in order to follow the damage under tensile deformation of poly(lactic acid). More recently, the damage mechanisms have been studied in the case of semi-crystalline (PA66⁴⁹) and amorphous polymers (cellulose acetate²⁷). Mourglia-Seignobos et al. studied the fatigue damage mechanisms of neat PA66⁴⁹. They proposed a quantitative mechanism of damage in this polymer: cavities of the order of 50 nm nucleate in the amorphous phase, in the equator of

spherulites. Breaking of the sample is the consequence of the accumulation of these defects and is not due to the propagation of a single crack. Charvet et al.²⁷ studied the microscopic mechanisms of damaging in plasticized cellulose diacetate (CDA) under tensile deformation. The authors observed a heterogeneous nucleation of cavities in the vicinity of pre-existing impurities, which growth is initially blocked by strain hardening. When the applied stress becomes sufficiently high, a fraction of these cavities grow faster until the failure of the sample.

The objective of this work is to study the damage mechanisms from the initiation until breaking of other amorphous and weakly semi-crystalline polymers: three different polyphthalamides (PPA), as well as polycarbonate (PC) and poly(methyl)methacrylate (PMMA). PC and PMMA are highly studied polymers known for their strain hardening behavior, especially in compression in the case of PMMA. PC presents a strong strain hardening regime, while PMMA presents a weaker strain hardening. The three polyamides of our study display also strain hardening⁵⁰. Our approach is similar to the approach used by Stoclet et al⁴⁸, Mourglia-Seignobos et al⁴⁹ and Charvet et al²⁷. We analyze damage by USAXS at different elongations during a uniaxial tensile test for all our samples. Measurements performed by USAXS allow to determine the evolution of the number density, volume fraction and size of damages during the tensile deformation. All this information allows us to describe the damage mechanism in the studied polymers until breaking when it takes place.

The manuscript is organized as follows. First we present the materials and methods (section 2). In section 3 we present the results. First, we present and discuss the mechanical properties of our samples including the strain hardening regime observed under tensile measurements with the three PPA, with PC and with PMMA. The tensile test at different temperatures permits to show different behaviors at low and high temperatures. At low temperatures, a fragile regime is highlighted, while at high temperatures a ductile regime can be observed. Our study of damage deals with polymers in their ductile regime. We discuss also the volume variations (section 3.2) of our samples under applied strain, which allows calculating the Poisson ratio of our polymers in the linear regime and its extension in the large amplitude deformation.

We measure the surface tension of our samples both before applied strain and far in the strain hardening regime (section 3.3). These two quantities are of interest for discussing qualitatively the cavitation processes or why they are inhibited in some cases and not in other cases. Then, scattered intensities obtained by USAXS measurements at different strain values are presented and modeled quantitatively (section 3.5) in order to describe the damage in the samples at different deformations. The corresponding damage mechanisms observed in PPA, PC and PMMA will be discussed. The results are discussed in section 4.

2 Materials and Methods

2.1 Material

Five different polymers are considered. We consider three semi-aromatic polyamides (PPA). These polymers are formed by copolymerization of PA6T and PA6I in different proportions. Monomers are obtained by the condensation reaction of hexamethylenediamine (HMDA) with a diacid: isophthalic (terephthalic) acid for the PA6I (PA6T) monomers. The resulting PPA can be amorphous or semi-crystalline depending on the proportion of the two different monomers¹. Semi-crystalline PPA are mainly based on PA6T, while the resulting copolymer is amorphous when the fraction of PA6I is larger than 55%⁶. Each of the studied PPA corresponds to a different fraction in PA6I or PA6T, indicated in Table 1 as well as their corresponding glass transition temperatures.

At large deformations, the studied PPA have a ductile behavior at temperatures above the brittle-ductile transition temperature T_{bd} . In this regime, failure –if any– takes place at a deformation larger than the deformation accessible within the testing machine, that is 60% of true strain of the necked part of the samples which has been the larger tested amplitude.

We study a Polycarbonate (PC) Makrolon GP clear 099 (Bayer), and a PMMA Plexiglas GS2458. Polycarbonate is a polymer that has been studied a lot from a mechanical point of view, but not studied with regard to damage to the best of our knowledge.

	Ratio PA6I/6T	Crystallinity (%)	T_g (°C)
Polyamide A	PA6I/6T 70/30	0	129.2
Polyamide B	PA6I/6T 50/50	4.3	130.2
Polyamide C	PA6I/6T 30/70	16.4	133.7
Polycarbonate	/	0	149.7
PMMA	/	0	97.56

Table 1 Glass transition temperatures (T_g) measured by DSC for all the considered polymers. The PA6I/6T ratio is given for all the PPA.

The glass transition temperature T_g was determined by Differential Scanning Calorimetry (DSC). T_g is similar for the three PPA and about 130°C. Like all semi-aromatic PPA with more than 55% of PA6I⁶, Polyamide A is amorphous. Polyamide B and C are both semi-crystalline, with a crystallinity ratio of 4.3% and 16.4%, respectively. Crystalline fractions were obtained by DSC using the following formula:

$$\chi_c = \frac{\Delta H_f^{measured}}{\Delta H_f^{100\%}}, \text{ where } \Delta H_f^{100\%} \text{ is the enthalpy of melting of a 100\% crystalline polymer. The enthalpy}$$

of melting is given in the literature for PA6,6 (188 J g⁻¹)⁷ and PA6,10 (207 J g⁻¹)⁷, but not for the crystalline PA6T part of Polyamide C. As a consequence, an average value of 200 ± 20 J g⁻¹ is used⁵¹. To provide an additional and independent measure for $\Delta H_f^{100\%}$, the crystalline fraction for PA6T was

determined by WAXS (Wide-Angle X-ray Scattering) experiments. The peaks obtained in WAXS were de-convoluted and the amorphous halo was subtracted from the crystalline peaks. The crystalline fraction

χ_{RX} was calculated using the formula: $\chi_{RX} = \frac{A_C}{A_C + A_A} \times 100$, with A_C and A_A the areas of crystalline and

amorphous parts, respectively. Then the enthalpy of melting of a 100% crystalline PA6T is calculated as

follow: $\Delta H_f^{100\%} = \frac{\Delta H_{DSC}}{\chi_{RX}}$ and is 196 J g^{-1} . WAXS measurements were performed on an Oxford Xcalibur Mova diffractometer in transmission mode at the Henri Longchambon Diffraction Center of Université de Lyon.

2.2 *Injection molding*

Two injection modes were defined. First, the process A: polymers were injection-molded into tensile specimens with a Billion select 100T injection press. Prior to molding, water content has been controlled by Karl Fischer in order to avoid hydrolysis or post-condensation reaction. Water content was found to be smaller than 700 ppm. Higher water content leads to hydrolysis and the molecular weight decreases. If the moisture content is lower than that of the chemical equilibrium, a post-condensation reaction with water formation and an increase of the molecular weight of the resulting polyamide may occur. Pellets were dried 24 hours at 110°C under vacuum before processing. Mold temperature was kept at 30°C . After molding, the samples were stored in sealed bags to maintain them dry. Tensile specimens dimensions were $150 \times 10 \times 4 \text{ mm}^3$ (ISO-527 norm). The process A concerns only polyamide A, polyamide B and polyamide C.

The injection process has an influence on mechanical properties of polymers, in particular on the skin-core effect due to flow during injection.⁵² This effect is present in the industrial process, due to a temperature gradient between the mold and the polymer melt (at higher temperature) during the injection process. A skin-core effect was observed for polyamide C by cross-polarized optical microscopy. Indeed, a birefringent character was observed between the skin and the core of the polymer. Samples of polyamide C were injection-molded with different mold temperatures (30 , 60 , 80 and 100°C). The storage modulus E' determined by DMTA at 1 Hz shows no difference regardless of the mold temperature ($E' = 3.1 \text{ GPa}$ at 25°C for the four mold temperatures). The temperature of the mold during the injection has no impact on the modulus E' . The degree of crystallinity remains low for Polyamide B and is homogeneous

over the thickness for the two semi-crystalline PPA (polyamide B and polyamide C), and was verified by DSC experiments. The skin-core effect observed for polyamide C only is related to shearing during the injection process and not to a difference in crystallinity within the material. The choice of setting the mold temperature at 30°C corresponds to an industrial injection process.

Second, the process B: polycarbonate (PC) and poly(methyl methacrylate) (PMMA) were bought in the form of plate (dimensions $500 \times 500 \times 5 \text{ mm}^3$ for PC and dimensions $200 \times 300 \times 5 \text{ mm}^3$ for PMMA). In order to have the same thickness as our home made samples, 0.5 mm were removed on each side of the plate thickness. Tensile bars (hourglass shape) with dimensions $92 \times 14 \times 4 \text{ mm}^3$ and with a radius of curvature larger than ISO-527 tensile specimens (71) were cut in the plates in the direction of injection, avoiding the edges of the plate. The specimen's geometry is designed specifically in order to study the strain hardening behavior of polymers.

2.3 *Characterization Methods*

2.3.1 Video-controlled tensile test

In order to characterize the Young modulus E , the yield stress σ_y and the strain hardening modulus E_{SH} of the studied polymers, tensile strength experiments were carried out on a Zwick/Roell Z050 universal testing machine equipped with a 50 kN load cell, a thermally controlled chamber and a non-contact extensometer (VidéoTraction®).²² The VidéoTraction® system is based on the measurement and regulation of the local deformation in a representative volume element (defined by several dot markers on the middle of the tensile specimen) and measures the true strain and the true stress during the test. The development of localization phenomena like necking is taken into account in the measured behavior²³. In polyamide A, B and C samples, the necking area is reproducible. The dot markers are placed in order to study this area. Samples were dried as molded (d.a.m.) and were strained at a constant true strain rate $\dot{\epsilon} = 1.10^{-3} \text{ s}^{-1}$ at different temperatures (between 23°C to 130°C, depending on the polymer, see Table

3). Each sample was conditioned 20 min in the temperature chamber before being tested. For each temperature, five samples were tested.

2.3.2 Determination of the surface tension of the different polymers

In order to determine the surface tension of our samples before deformation and during strain hardening, we measure the contact angle of droplets deposited on the polymer surfaces. A tensiometer (drop shape analyzer) DSA100 (Krüss) was used, at 23°C. This tensiometer makes it possible to measure the contact angles by optical methods (drop deposit). Two liquid probes were used: water and diiodomethane. The surface tension γ_L of water and its dispersive component γ_L^d are respectively 72.8 mJ.m⁻² and 21.8 mJ.m⁻²^{53,54}. For diiodomethane, γ_L and its non-dispersive component γ_L^{nd} are respectively 50.8 mJ.m⁻² and 2.3 mJ.m⁻²⁵³.

Surface tension is the sum of a dispersive component (γ_S^d , London forces) and a non-dispersive or polar component (γ_S^{nd}):

$$\gamma_S = \gamma_S^d + \gamma_S^{nd} \quad (1)$$

The contact angle of a droplet deposited on the polymer sample is given by the relation:

$$\gamma_L(1 + \cos \theta) = 2\sqrt{\gamma_S^d \times \gamma_L^d} + 2\sqrt{\gamma_S^{nd} \times \gamma_L^{nd}} \quad (2)$$

Using Equation 1 and Equation 2, it is possible to calculate the surface tension of the polymer.

2.3.3 Microscopic observations

In order to observe the damage morphologies, Scanning Transmission Electron Microscopy (STEM) was used. Tensile specimens were cut in the center region below the failure surface for PMMA or polycarbonate, or in the center region where the dot markers of the VidéoTraction were present, as shown in Figure 1. All samples were ultramicrotomed to a specimen thickness of 150 nm using a Reichert Ultracut S microtome at room temperature with a diamond knife in order to obtain a mirror surface.

Sections were picked-up on a copper grid (200 mesh) and imaged using a Zeiss Ultra 55 STEM with an annular bright-field (or dark-field if necessary). Typical operating conditions for bright-field and dark-field STEM imaging include an accelerating tension of 20 kV, a diaphragm aperture size at 20 μ m and a working distance of about 6 mm.

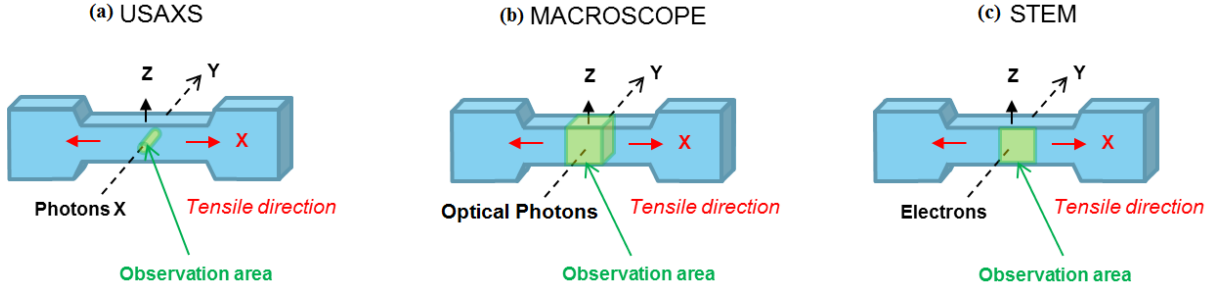


Figure 1 Schematic representation of the area observed by (a) USAXS, (b) Optical microscopy and (c) Scanning Transmission Electron Microscopy.

2.3.4 Ultra-small angle X-ray scattering (USAXS) measurements

All the scattering data are expressed in terms of the modulus of the scattering vector $q = 4\pi\sin(\theta)/\lambda$, with λ the X-ray wavelength and 2θ the scattering angle. If we consider a homogeneous polymer matrix, with spherical objects (impurities, particles or cavities) of radius R randomly dispersed in the matrix, the resulting scattered intensity shows two characteristic regimes⁵⁵. At low q values ($qR < 1$), the scattered intensity can be described by the so-called Guinier regime⁵⁶ with $I(q) \cong G \exp\left(-\frac{q^2 R^2}{5}\right)$ where the prefactor G is equal to $G = \beta^2 \rho_e^2 N V^2$ with V the volume of the object defined by $V = 4\pi R^3/3$. At high q values ($qR > 1$), the scattered intensity can be described by the Porod regime⁵⁷ with $I(q) \cong B q^{-4}$, where the prefactor B of the power law can be related to the surface area of the particles and is equal to $B = 2\pi\beta^2 \rho_e^2 N S$. $\beta^2 = 7.8 \times 10^{-24} \text{mm}^2$ is the electron cross section, ρ_e is the average electron density contrast between the polymer matrix and the objects and N is the number density of the objects. $S = 4\pi R^2$ is the surface area.

Beaucage et al⁵⁷ have proposed a global unified scattering function. This function gives an approximation of the scattering of spherical particles which covers the Guinier and Porod regimes:

$$I(q) = G \exp\left(\frac{-q^2 R^2}{5}\right) + B \left(\frac{\left(\operatorname{erf}\left(\frac{qR}{\sqrt{10}}\right)\right)^{12}}{q^4} \right) \quad (3)$$

where $\operatorname{erf}(x)$ is the error function defined by⁵⁸: $\operatorname{erf}(x) = \frac{2}{\sqrt{\pi}} \int_0^x e^{-t^2} dt$.

The error function approaches zero when q approaches zero, and 1 when q tends to infinity.

The global unified scattering function is only valid for a single polydisperse level of spherical primary particle. If the material contains several polydisperse levels of different cavities or structures, the contributions of each have to be integrated and added in the global scattering function⁵⁵.

The electron density of a polymer i can be expressed by:

$$\rho_i = \frac{n_i \times d_i \times N_A}{M_i} \quad (4)$$

with n_i the number of electrons per repeat unit in the polymer, d_i the density of the polymer, N_A the Avogadro's number ($N_A = 6.022 \times 10^{23} \text{mol}^{-1}$) and M_i the molar mass of the repeat unit of the polymer.

From Equation 4, the electron density of each polymer is determined and is available in Table 2.

	n_i	d_i (g.mm ⁻³)	M_i (g.mol ⁻¹)	ρ_i (mm ⁻³)
PPA	132	1.18x10 ⁻³	246.3	3.81x10 ²⁰
PC	134	1.19x10 ⁻³	254.3	3.78x10 ²⁰
PMMA	54	1.18x10 ⁻³	100.0	3.84x10 ²⁰

Table 2 Number of electrons per repeat unit n_i , density d_i , molar mass of the repeat unit M_i and electron densities of the different studied polymers.

USAXS experiments were carried out on the High brilliance Beamline (ID02) at the European Synchrotron Radiation Facility (ESRF, Grenoble, France). The X-ray energy was set to 12.46 keV (which corresponds to $\lambda = 0.995 \text{ \AA}$). The region illuminated by the X-ray beam was about $100 \times 100 \mu\text{m}^2$. A 2D-detector Rayonix MX-170HS (X-ray area: $170 \times 170 \text{ mm}^2$) was used. Three sample-to-detector distances d from 1m to 31m were used. When $d = 31\text{m}$, the accessible q range is $10^{-3}\text{nm}^{-1} < q < 10^{-2}\text{nm}^{-1}$. For $d = 8\text{m}$, the q range is $10^{-2}\text{nm}^{-1} < q < 10^{-1}\text{nm}^{-1}$. For $d = 1\text{m}$, the q range is $10^{-1}\text{nm}^{-1} < q < 10 \text{ nm}^{-1}$. For each sample, five measurements were made, with an acquisition time of 5 s. The X-ray scattering data were reduced (average of the 5 measures, integration, normalization, subtraction of the empty frames) using SAXSutilities software, developed for the ID02 beamline by Sztucki et al⁵⁹.

Additional X-ray scattering data were collected on the SWING beamline at SOLEIL, the national French synchrotron facility (Saint-Aubin, France). The beam energy was set to 12 keV (which corresponds to $\lambda = 1.033 \text{ \AA}$). A Dectris detector Eiger 4M was used (pixel size: $75 \times 75 \mu\text{m}^2$, dimension: 1035×1083). The q range was set to $0.00148 - 1.8844 \text{ nm}^{-1}$. The low q region was explored using a sample-to-detector distance of 6.18m. For each sample, five measurements were made, with an acquisition time of 600 ms.

All data were normalized by the thickness of the sample and plotted as a function of the scattering vector q .

3 Results and Discussions

3.1 Tensile behavior

The true stress – strain curves obtained under uniaxial tensile test at a true axial strain rate $\dot{\epsilon} = 1.10^{-3}s^{-1}$ are shown in Figure 2 for the three PPA and Figure 3 for polycarbonate and PMMA. The behavior of all polymers is typical of glassy polymers. Stars in Figure 2 and Figure 3 indicate the strain values where USAXS measurements were performed. We studied the behavior of the considered polymers in their fragile and ductile regimes, notably through the determination of their brittle-to-ductile transition T_{bd} . Polyamides A and B, as well as polycarbonate are ductile at 23°C, while polyamide C and PMMA are ductile above 110°C and 70°C, respectively. The study of the damage of these polymers will be done at a temperature higher than their brittle-ductile transition.

The Young modulus E is calculated from the tangent line in the elastic domain (between 0.05% and 0.25% of true strain) and characterizes the stiffness of the polymer. The yield stress σ_y is defined as the observed maximum stress at the end of the viscoelastic regime. After yield, a small drop of the stress can be observed (Figure 2-a for example). It is called strain softening. All the studied polymers show a strain hardening regime. This regime continues until the specimens reach their critical stress value at failure for polycarbonate and PMMA. Polyamide A, B and C do not break within the accessible deformation range of our tensile machine. These three PPA deform by necking, which appears just after the yield stress. Polymers are studied above their brittle-ductile transition regarding damaging.

All the experimental values determined from the curves in Figure 2 and Figure 3 are reported in Table 3.

Materials	°C	E (MPa)	σ_y (MPa)	E_{SH} (MPa)	ϵ_r (%)	T_{BD} (Tensile test) (°C)
Polyamide A	60	2521 ± 434	70.1 ± 0.5	48 ± 6	N/A	$< -40^\circ\text{C}$
Polyamide B	60	2980 ± 293	68.6 ± 0.3	52 ± 7	N/A	$< -40^\circ\text{C}$
Polyamide C	130	1830 ± 354	29 ± 0.5	37.5 ± 5	N/A	110°C
Polycarbonate	23	2771 ± 310	66.9 ± 2	53.8 ± 11	46 ± 2	$< 0^\circ\text{C}$
PMMA	80	1297 ± 126	21 ± 1	7.1 ± 2	90 ± 3	70°C

Table 3 Mechanical properties of the different studied polymers. Data obtained from Figure 2 and Figure 3. The strain hardening modulus E_{SH} is measured by the slope between the strain range 30-35% in each curve.

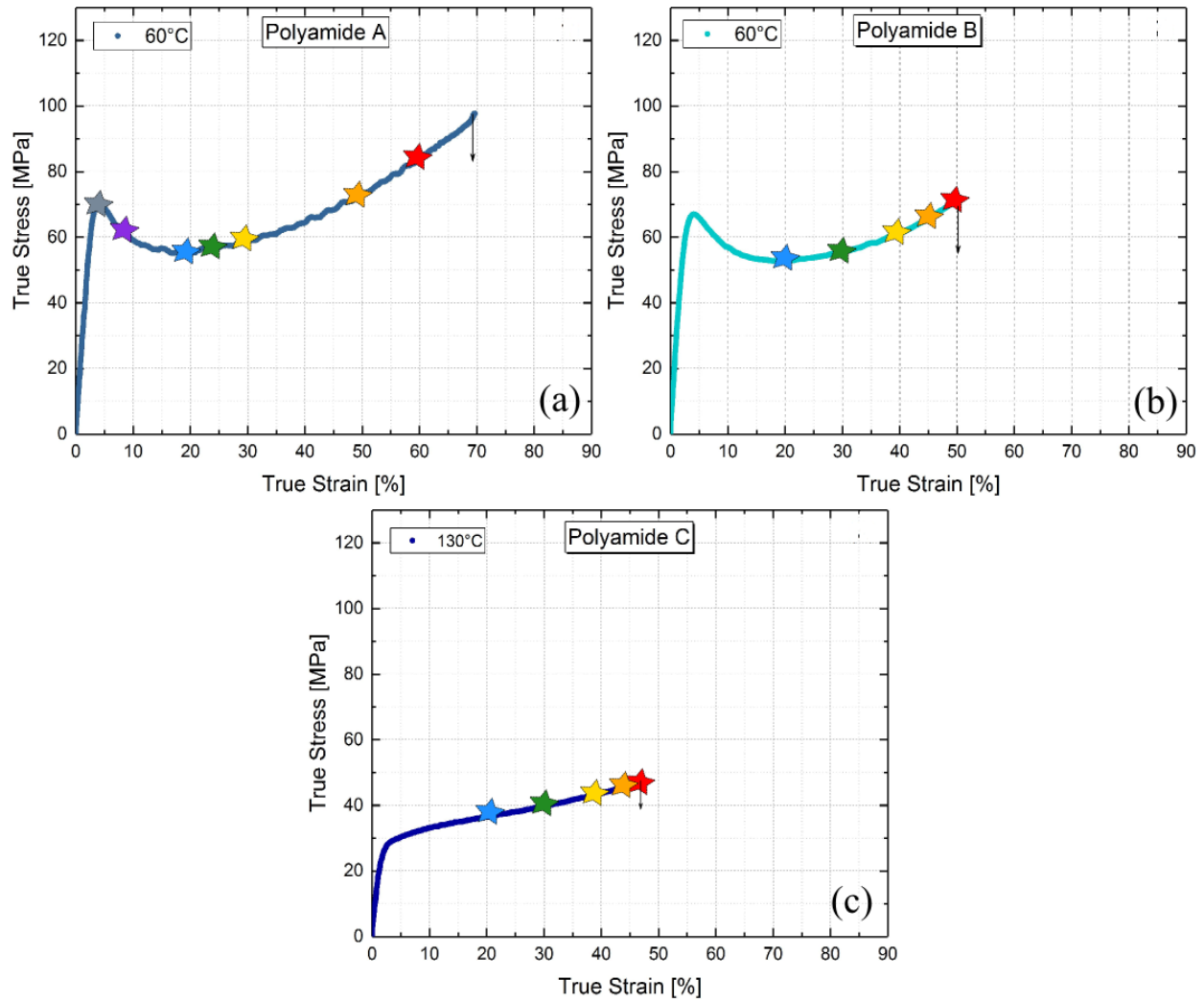


Figure 2 Tensile true stress – true strain curves obtained at 0.001 s^{-1} for each PPA: (a) polyamide A, (b) polyamide B and (c) polyamide C. Stars indicate the USAXS measurements, arrows indicate unbroken samples.

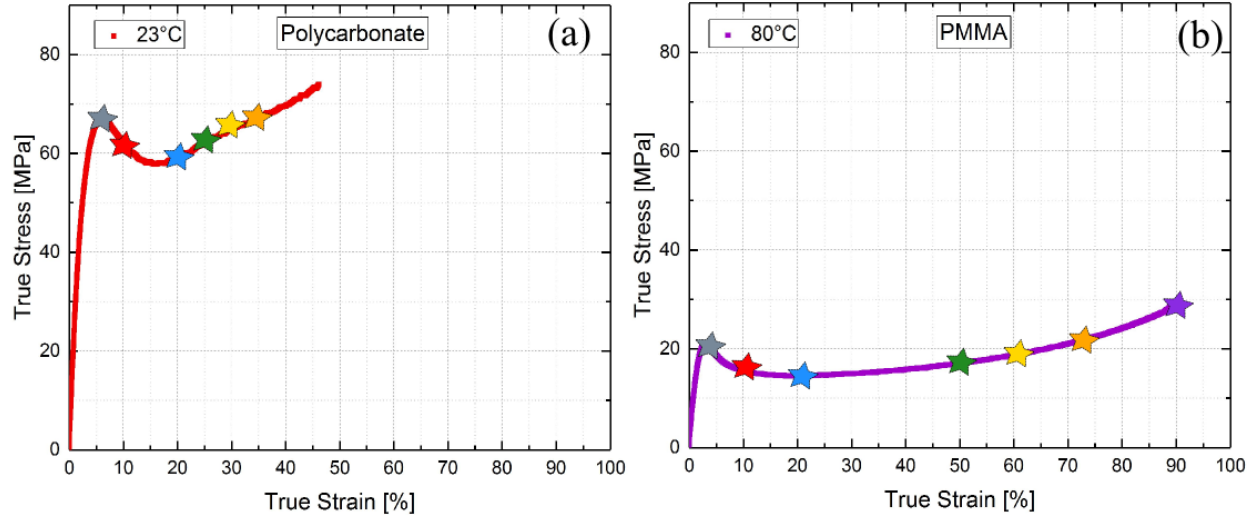


Figure 3 Tensile true stress – true strain curves obtained at 0.001 s^{-1} for Polycarbonate (a) and PMMA (b). Stars indicate the USAXS measurements.

3.2 Volume variation

The volume variation expressed by the term V/V_0 is calculated thanks to the longitudinal strain and the transverse strains (deformation of the sample in thickness and width) measured by VideoTraction. Figure 4 shows the volume variation V/V_0 with the true strain for each polymer at different temperatures.

Polyamide C, PMMA and polycarbonate display the same tendency: the volume increases with the deformation, up to 5% for polyamide C, 1.5% for PMMA and 3% for polycarbonate at 40% of true strain. For polyamide A, at 60°C , the volume increases by approximately 1% at 5% of deformation and then no longer varies with the deformation. For polyamide B at 60°C , the volume increases up to 7% from about 7% to 35% true strain, and then decreases.

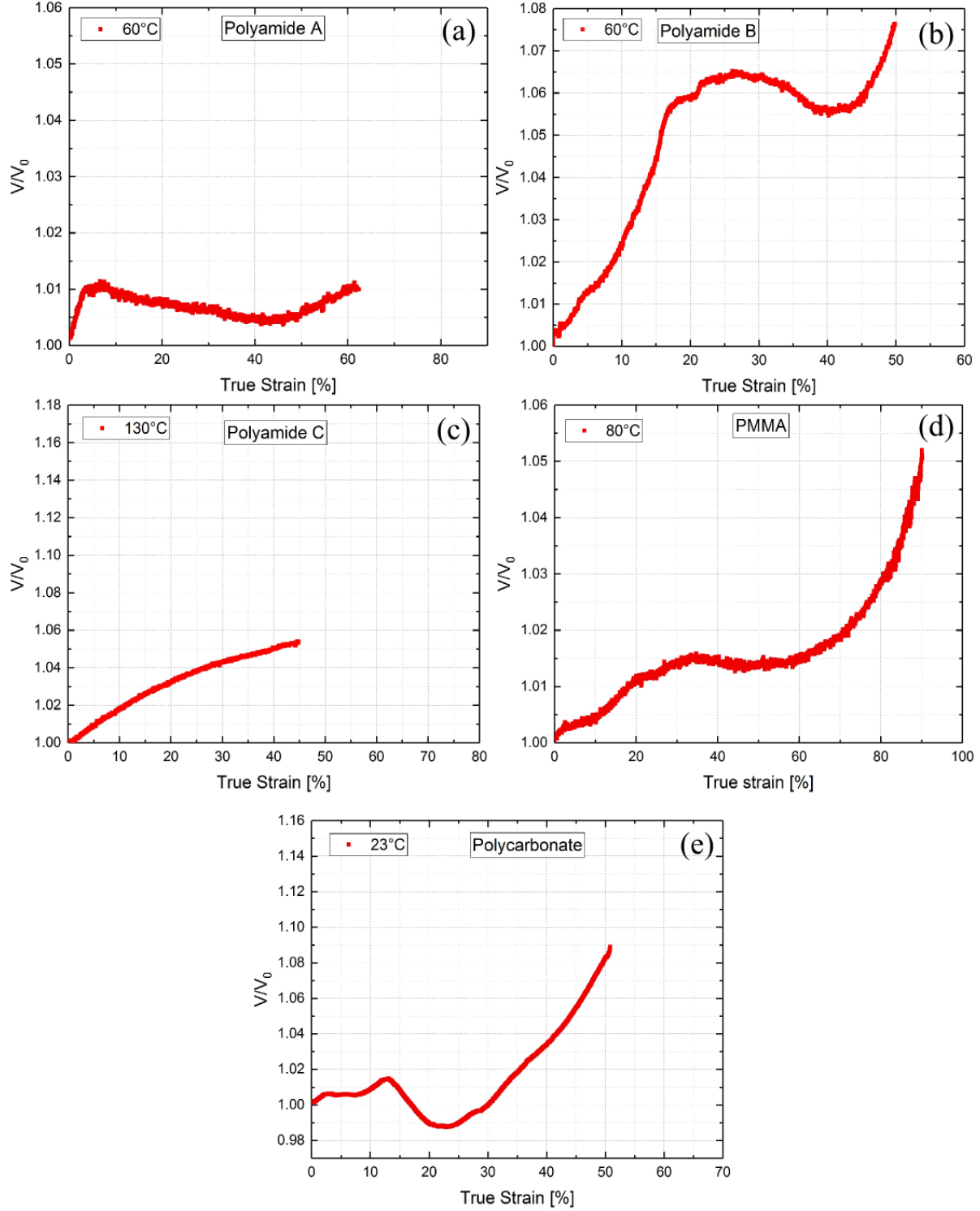


Figure 4 Evolution of the volume variation V/V_0 with the true strain for each polymer at different temperatures. (a) Polyamide A at 60°C; (b) polyamide B at 60°C; (c) polyamide C at 130°C; (d) PMMA at 80°C and (e) polycarbonate at 23°C.

3.3 Surface tension

Contact angles were measured before and after deformation on the polymers to determine surface tensions, γ_s . To do this, water and diiodomethane were used. The measured contact angles for each polymer before and after tensile deformation are shown in Table 4.

	Before deformation		After deformation		
	Water	Diiodomethane	True strain (%)	Water	Diiodomethane
Polyamide A	59.4°	36.4°	60 %	47.3°	19.4°
Polyamide B	61.2°	59.1°	50 %	47.5°	45.3°
Polyamide C	62.5°	58.9°	60 %	47.5°	46.4°
Polycarbonate	84.5°	54.5°	45 %	68.9°	40.6°
PMMA	64.1°	56.2°	90 %	55.2°	51.4°

Table 4 Contact angles measured with two liquids: water and diiodomethane, before and after tensile deformation.

The contact angles measured with water are higher than with diiodomethane. With the measured contact angles, and with Equations 1 and 2, the surface tension before and after deformation can be calculated for each polymer. Table 5 shows the calculated surface tensions.

	Before deformation			After deformation			
	γ_s^d (mJ/m ²)	γ_s^{nd} (mJ/m ²)	γ_s (mJ/m ²)	True strain (%)	γ_s^d (mJ/m ²)	γ_s^{nd} (mJ/m ²)	γ_s (mJ/m ²)
Polyamide A	43.3	11.5	54.8	60 %	50.2	15.3	65.5
Polyamide B	30.5	15.5	46.0	50 %	38.6	20.0	58.6
Polyamide C	30.6	14.7	45.3	60 %	38.0	20.3	58.3
Polycarbonate	33.2	3.3	36.5	45 %	41.1	7.5	48.6
PMMA	32.2	13.1	45.3	90 %	35.1	17.1	52.2

Table 5 Dispersive and non-dispersive components of the surface energy of each polymer (γ_s^d and γ_s^{nd}), and surface tension (γ_s) before and after tensile deformation.

Figure 5 shows a representation of the surface tension γ_s for each polymer before and after deformation.

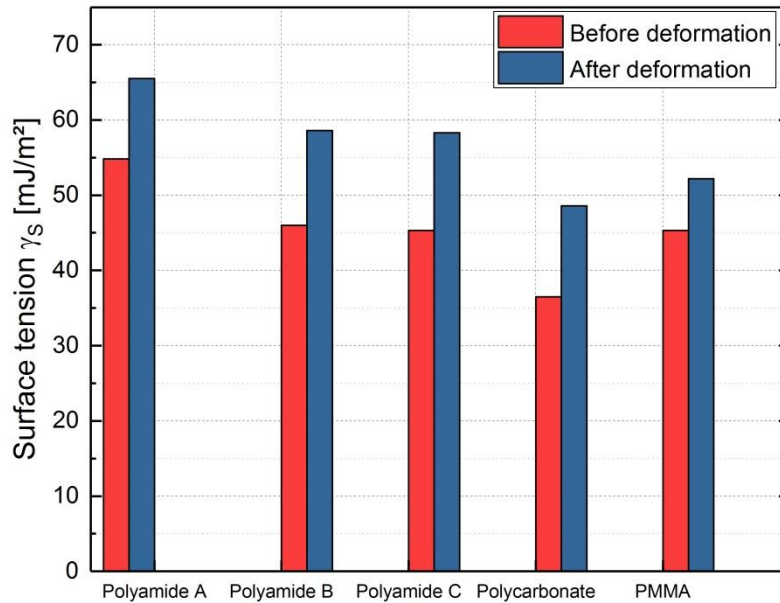


Figure 5 Surface tension γ_s of each polymer before and after tensile deformation

After deformation, the surface tension is higher for all the studied polymers, as observed in Figure 5. Polyamide A has a surface tension of 65.5 mJ/m² after deformation, which is more than the other two PPA (polyamide B and polyamide C) which have a surface tension after deformation of 58.6 mJ/m² and 58.3 mJ/m² respectively. The studied polycarbonate and PMMA have a surface tension after deformation of 48.6 mJ/m² and 52.2 mJ/m² respectively.

3.4 *Microscopic observations of damage*

Microscopic observations have been done by macroscope, optical microscopy (OM) and scanning transmission electron microscopy (STEM), in the useful area (schematized in Figure 1). PMMA has a high sensitivity to electron irradiation. It is very difficult to perform electron microscopic observation. The focus must be done quickly in order to prevent polymer degradation³⁴.

No cavities are observed on all the samples before tensile experiment by macroscope, OM or STEM.

All the deformed samples were analyzed by STEM but no damage could be observed on the micrographs. It is supposed that the size of damage is not compatible with the microscope resolution, or the contrast between structural damage (homogeneous crazes) and the polymer matrix is too small. USAXS measurements permit a quantitative study of the damages. Note that it was also the case in the study of Mourglia-Seignobos et al⁴⁹ for PA66 during fatigue solicitation. Damage could be characterized in USAXS experiments in the early stages but not by electron microscopy.

With all the studied polymers, we were not able to observe in microscopy the damage morphology. Based on literature (Kramer, Michler^{30,34,36,38}) and on the recent study by Charvet et al²⁷, the different types of damage expected in the studied polymers are shown schematically in Figure 6.

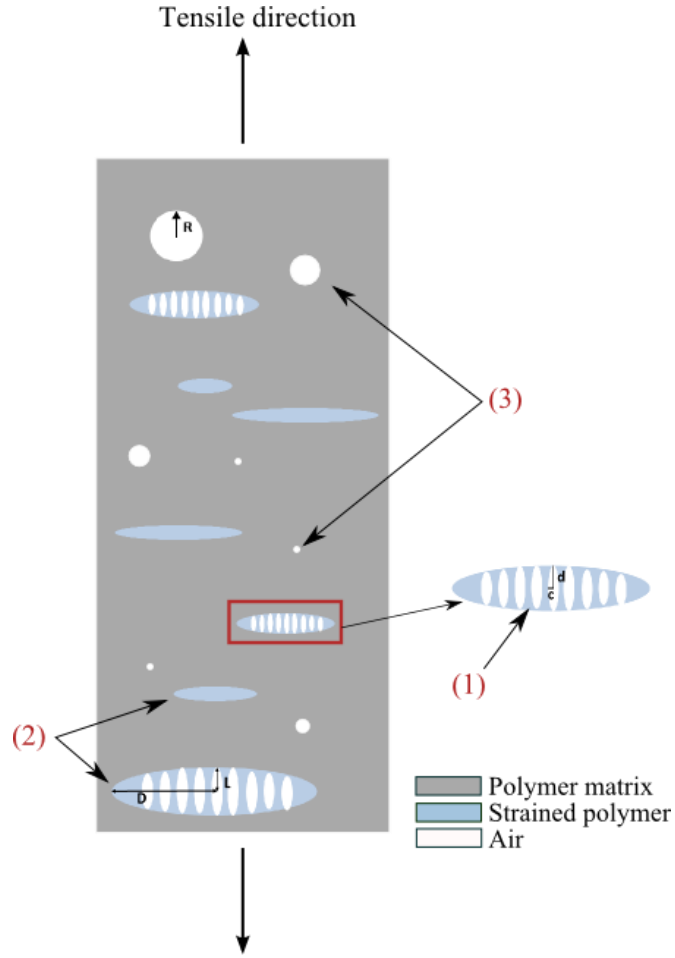


Figure 6 Representation of the different damage morphologies expected in the studied polymers. Type (1) damages correspond to small elongated cavities (interior structure of a craze, between fibrils) with dimensions d along the radius of the fibril and c corresponding to the small radius of the fibril; Type (2) damages correspond to homogeneous and fibrillated crazes (larger scale) with dimensions D corresponding to the large radius of the ellipsoid and L corresponding to the small radius of the ellipsoid and type (3) damages correspond to large cavities of radius R , induced by injection process.

The scattered intensities measured by USAXS experiments are analyzed thanks to this diagram, according to the objects encountered. The first category of defects corresponds to small elongated cavities (interior structure of crazes), with d corresponding to the long radius of the fibril and c corresponding to the small radius of the fibril, as shown in Figure 6. The second category corresponds to homogeneous and fibrillated crazes with the dimensions D corresponding to the large radius of the ellipsoid and L

corresponding to the small radius of the ellipsoid. The last category, 3, corresponds to large cavities induced by injection process.

3.5 Characterization of damage by Ultra-small Angle X-ray Scattering (USAXS)

All the studied polymers were analyzed by Ultra-small angle X-ray Scattering (USAXS) with a 2D detector, after tensile experiments at several temperatures. During the USAXS experiments, the scattered intensity is initially isotropic, as observed in Figure 7-a. The scattered intensity becomes anisotropic with the deformation: the observed diffusion is not homogeneous, as seen in Figure 7-b-c.

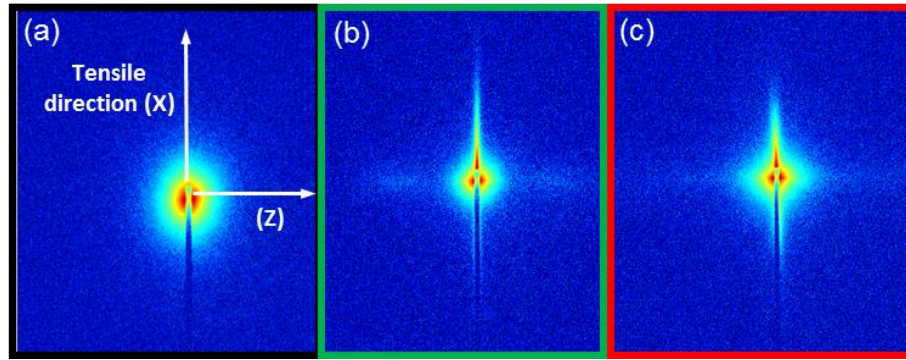


Figure 7 2D USAXS patterns for polyamide A before tensile deformation (a), and after tensile experiment at 60°C: (b) 25% of deformation and (c) 60% of deformation.

3.5.1 Fitting equations

From the 2D patterns obtained in USAXS experiments, the scattered intensities are integrated along the tensile direction (*parallel*), in an interval of azimuth angle $[-10, +10^\circ]$, and perpendicular to the tensile direction (*perpendicular*), in an interval of azimuth angle $[80, 100^\circ]$. Figure 8 gives a schematic representation of the general form of the global scattered intensities in both parallel direction (axis x, blue curve) and perpendicular direction (axis z, green curve). We obtained the restricted scattered intensities in both directions.

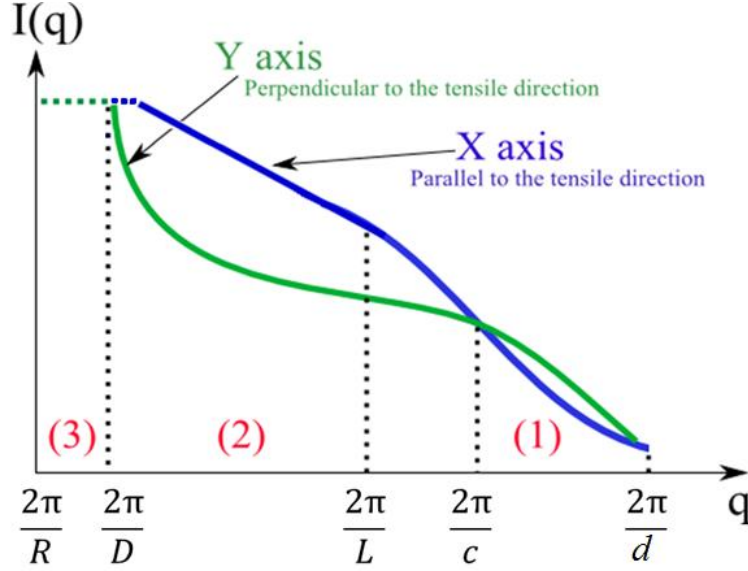


Figure 8 Schematic representation of the general form of the global scattered intensities of a polymer with different damage morphologies. The contributions of different types of defects are shown: 1: small elongated cavities (interior structure of crazes), 2: homogeneous and fibrillated crazes and 3: large cavities induced by injection process.

As schematized in Figure 8, three regions can be determined in the scattered intensities of our polymer samples. At high q values, for $q > 2\pi/c$ (region 1 in Figure 8), the scattering is due to small elongated cavities inside the fibrillated crazes. The scattering pattern of these cavities is anisotropic. Uniaxial ellipsoids elongated along the tensile direction are used to model the cavities. The long radius of the ellipsoids in the direction parallel to the tensile direction (X axis) is defined as d , and the short radius of the ellipsoids in the direction perpendicular to the tensile direction (Z axis) is defined as c . The scattered intensities resulting in both directions (parallel and perpendicular to the tensile direction) can be expressed by Equations 5 and 6.

$$I_{parallel_1}(q) = \beta^2 \rho_{pol}^2 V_1^2 N_1 \left(\exp\left(\frac{-q^2 d^2}{5}\right) + 4.5 \frac{\text{erf}\left(\frac{qd}{\sqrt{10}}\right)^{12}}{(qd)^4} \right) \quad (5)$$

$$I_{perpendicular_1}(q) = \beta^2 \rho_{pol}^2 V_1^2 N_1 \left(\exp\left(\frac{-q^2 c^2}{5}\right) + 4.5 \frac{\text{erf}\left(\frac{qc}{\sqrt{10}}\right)^{12}}{(qc)^4} \right) \quad (6)$$

where $V_1 = 4\pi dc^2/3$ is the volume of small elongated cavities, and N_1 is the number density of these small elongated cavities. The volume fraction is expressed by $\phi_1 = N_1 V_1$.

In the region 2, q is in the range $2\pi/D < q < 2\pi/c$. In this region, small isotropic and elongated cavities described above are unresolved and the scattering reveal only the global craze structure. Crazes are filled with polymer with a volume fraction of air ϕ . The contrast factor can be written as $\rho_e^2 = \phi^2 \rho_{pol}^2$ where ρ_{pol} is the average electron density of the polymer matrix. We consider the value $\phi = 0.25$ which is coherent with the cavities polymer volume fraction used by Mourglia et al⁴⁹ in polyamide and with the volume fraction of air within a fibrillar craze found by Michler et al³⁴ in polystyrene. Crazes are modeled by uniaxial ellipsoids with radius (half thickness) L along the tensile direction and larger radius D in the perpendicular direction. According to the work of Charvet et al on CDA²⁷, the microscopic observations showed a broad distribution for the size of crazes. To describe the resulting scattered intensity, some hypotheses must be done. We assume that the larger radius D (respectively L) varies between extremum values D_{min} and D_{max} (respectively L_{min} and L_{max}) and that D is a linear function of L as given in Equations 7 to 9:

$$D(L) = \epsilon L + \beta \quad (7)$$

with:

$$\epsilon = \frac{D_{max} - D_{min}}{L_{max} - L_{min}} \quad (8)$$

and

$$\beta = \frac{L_{max}D_{min} - D_{max}L_{min}}{L_{max} - L_{min}} \quad (9)$$

We assume that the size distribution $P(L)$ (where $P(L)dL$ denotes the number of cavities per unit volume with a size comprised between L and $L + dL$) can be described by a power law:

$$P_2(L) = P_2 L^{-\alpha} \quad (10)$$

The distribution $P(L)$ is normalized so that the number density of crazes of type 2 is given by:

$$N_2 = \int_{L_{min}}^{L_{max}} P_2(L) dL \quad (11)$$

The corresponding volume fraction of crazes ϕ_2 is given by the following equation:

$$\phi_2 = \int_{L_{min}}^{L_{max}} V_2(L) P_2(L) dL \quad (12)$$

Where $V_2 = 4\pi LD^2/3$ is the ellipsoid volume.

In region 2, the scattered intensity in both parallel and perpendicular directions is expressed by the following equations:

$$I_{parallel_2}(q) = \beta^2 \rho_{pol}^2 \varphi^2 \int_{L_{min}}^{L_{max}} V_2^2 \left(\exp\left(\frac{-q^2 L^2}{5}\right) + 4.5 \frac{\text{erf}\left(\frac{qL}{\sqrt{10}}\right)^{12}}{(qL)^4} \right) P_2(L) dL \quad (13)$$

$$I_{perpendicular_2}(q) = \beta^2 \rho_{pol}^2 \varphi^2 \int_{L_{min}}^{L_{max}} V_2^2 \left(\exp\left(\frac{-q^2 D^2}{5}\right) + 4.5 \frac{\text{erf}\left(\frac{qD}{\sqrt{10}}\right)^{12}}{(qD)^4} \right) P_2(L) dL \quad (14)$$

In the region 3 (Figure 8), at low q values ($q < 2\pi/D$), the scattered intensity has always been isotropic in our experiments. The scattered intensity observed comes from the response of large spherical cavities formed during the injection process. The radius of these cavities is comprised between R_{min} and R_{max} . The size distribution is expressed by a power law as in Equation 15:

$$P_3(R) = P_3 R^{-\alpha_1} \quad (15)$$

The scattered intensity is expressed as:

$$I_3(q) = \beta^2 \rho_{pol}^2 \int_{R_{min}}^{R_{max}} V_3^2 \left(\exp\left(\frac{-q^2 R^2}{5}\right) + 4.5 \frac{\text{erf}\left(\frac{qR}{\sqrt{10}}\right)^{12}}{(qR)^4} \right) P_3(R) dR \quad (16)$$

With V_3 , the volume of spherical cavities of radius R . Note that in this region, we don't know if the large spherical cavities formed during injection are empty. If they are empty, the volume fraction of air ϕ must be used. This would change the volume fraction of the cavities. Note however that the types of cavities were observed to be empty for CDA²⁷.

The number density of large cavities N_3 is given by the following equation:

$$N_3 = \int_{R_{min}}^{R_{max}} P_4(R) dR \quad (17)$$

The corresponding volume fraction ϕ_3 is given by Equation 18:

$$\phi_3 = \int_{R_{min}}^{R_{max}} V_3(R) P_3(R) dR \quad (18)$$

In both directions, the global scattered intensity is the sum of all contributions⁵⁵.

$$I_{parallel}(q) = I_0(q) + I_{parallel_1}(q) + I_{parallel_2}(q) + I_3(q) \quad (19)$$

$$I_{perpendicular}(q) = I_0(q) + I_{perpendicular_1}(q) + I_{perpendicular_2}(q) + I_3(q) \quad (20)$$

Where $I_0(q)$ is the incident beam intensity.

Figure 9 shows two examples of curves fitted thanks to Equations 19 and 20. Both parallel and perpendicular curves to the tensile direction were fitted together. All the results were fitted in the same way.

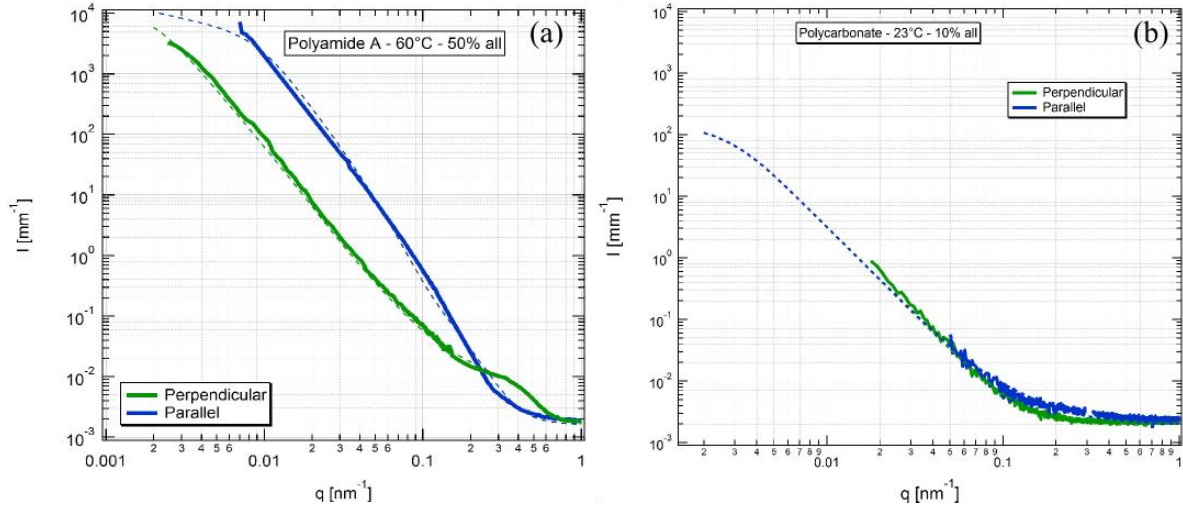


Figure 9 USAXS scattered intensities in the directions parallel (blue) and perpendicular (green) to the tensile direction on polyamide A at 60°C and 50 % of strain (a) and on polycarbonate at 23°C and 10 % of strain (b). The solid curve represents the experimental data, and the dotted curve represents the fit.

3.5.2 Before tensile experiments

In Figure 10 and Figure 11, the restricted scattered intensities in the parallel (blue curve) and perpendicular (green curve) directions to the injection direction are plotted for the three PPA (Figure 10) and for polycarbonate and PMMA (Figure 11) before tensile experiment. The difference in scattering intensities between the parallel direction and the perpendicular direction is due to cavities which nucleate on impurities during the injection process as was assumed by Charvet et al²⁷. Using Equation 16, both directions can be fitted. The distribution of the sizes of cavities is modelled with an exponent $\alpha=3.8$. Before tensile experiment for polyamide A, the signal is higher in the parallel direction to the perpendicular direction: we observe cavities oriented in the perpendicular direction. For polyamide B and polyamide C, a small bump in the q range 0.1 to 1 nm^{-1} is observable. This signal can be assimilate to cavities on the order of 10 nm oriented in the direction parallel to the injection. For the other polymers, the signal can be considered as almost isotropic. The volume fraction of initial damages ϕ_i , the number of initial damages per unit volume N_i , the size R_{\min} and R_{\max} of each polymer are given in Table 6.

	R_{\min} (nm)	R_{\max} (nm)	Volume fraction ϕ_i	Number of initial damage N_i (mm^{-3})
Polyamide A	13	1500	9.0×10^{-6}	1.1×10^9
Polyamide B	1	1000	3.1×10^{-5}	2.0×10^{10}
Polyamide C	10	1200	4.0×10^{-5}	1.0×10^{11}
Polycarbonate	1	1000	1.9×10^{-6}	3.9×10^5
PMMA	5	500	1.9×10^{-6}	4.2×10^7

Table 6 Size and volume fractions of initial damages corresponding to fitting parameters used for each polymer before tensile deformation in Figure 10 and Figure 11, $\alpha=3.8$.

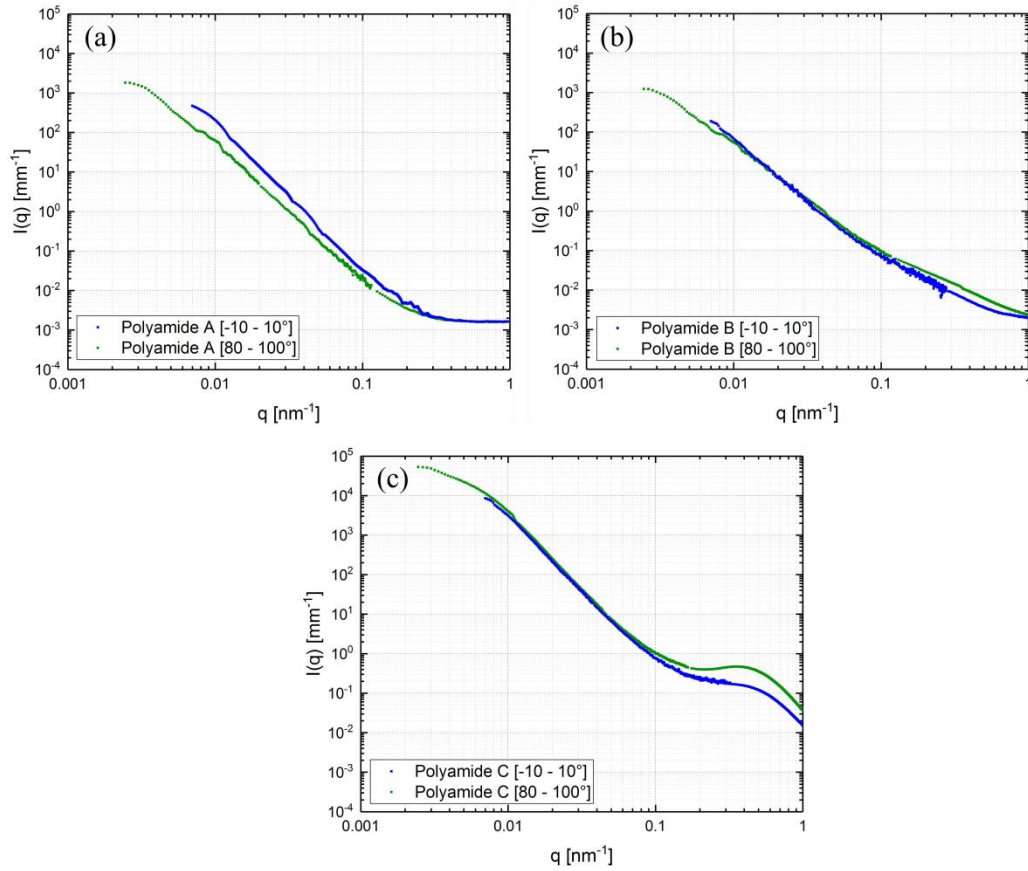


Figure 10 Restricted scattered intensities in both parallel (blue curve) and perpendicular (green curve) directions to the injection direction obtained by USAXS experiments on (a) polyamide A; (b) polyamide B and (c) polyamide C.

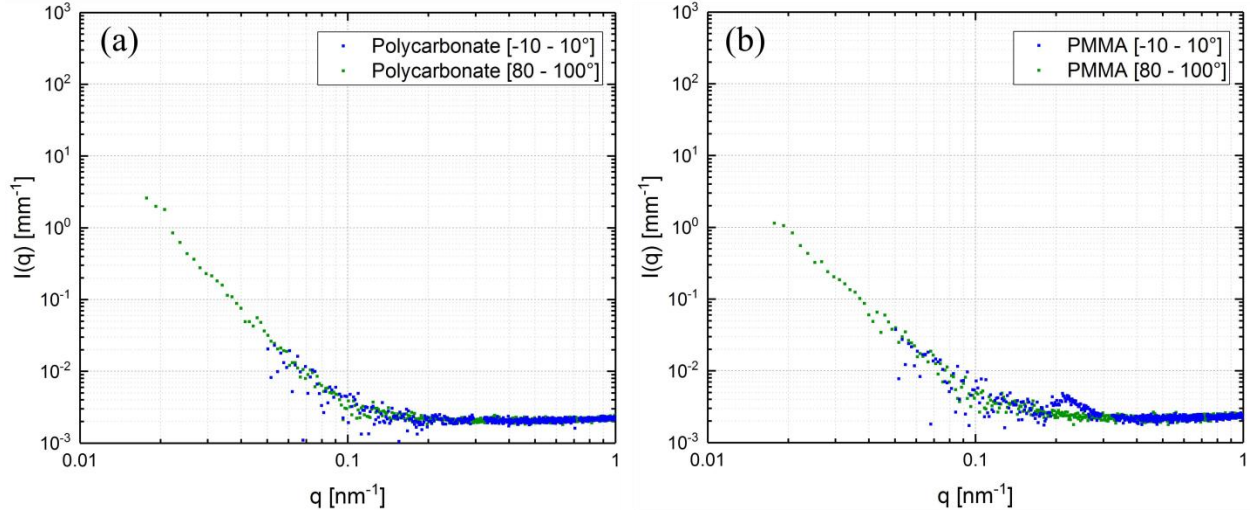


Figure 11 Restricted scattered intensities in both parallel (blue curve) and perpendicular (green curve) directions to the injection direction obtained by USAXS experiments on (a) polycarbonate and (b) PMMA.

3.5.3 Evolution of damage under tensile deformation:

The aim of the characterization of damage using USAXS experiments is to determine the mechanisms of initiation and propagation of damages, under uniaxial tensile deformation. In order to analyze a wide range of deformation, USAXS measurements were performed at different strain levels, as indicated by stars in Figure 2 and Figure 3.

3.5.3.1 Behavior under tensile deformation of polyamide A

Figure 12 shows both parallel and perpendicular scattered intensities at different strain levels at 60°C for polyamide A. The experimental data are fitted by global scattered intensity given by Equations 19 and 20. Thanks to the analysis of the experimental data, the size and the volume fraction of each typology of damage can be determined. All the adjustable parameters are given in Table 7.

At a temperature of 60°C and at small q values, the scattered intensities parallel to the tensile direction increase with deformation but do not evolve after 9% of deformation. The scattered intensity in the direction parallel to the deformation is about one decade higher than that in the direction normal to the

deformation. On the contrary, the scattered intensities perpendicular to the tensile direction remain constant. This evolution corresponds to the growth of elongated cavities oriented in the direction normal to the direction of traction.

The damage mechanisms of polyamide A during tensile deformation at 60°C can be defined by 2 regimes. The first regime is visible at high q values. In this regime, damages are initiated by the nucleation of small crazes, occurring before 9% of true strain, as visible on Figure 12-b (bump at $q > 0.1 \text{ nm}^{-1}$). These nucleated crazes remain small, with a maximal size of 100 nm in length (Table 7). The volume fraction of these crazes increases with deformation, from 2.0×10^{-6} to 1.4×10^{-5} .

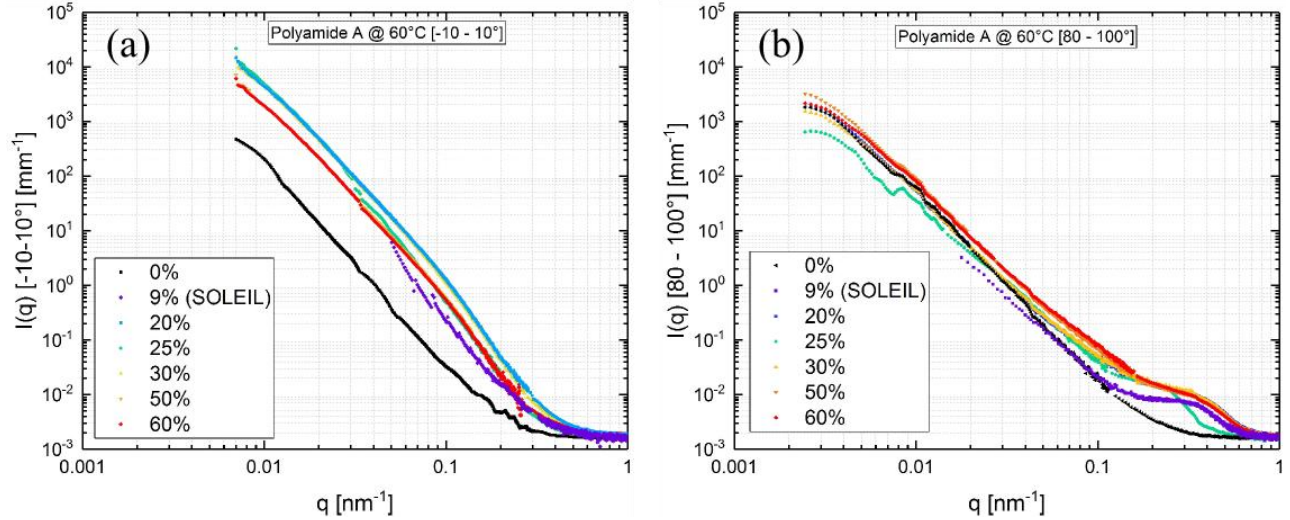


Figure 12 Restricted scattered intensities in the parallel direction (a) and perpendicular direction (b) to the tensile direction obtained by USAXS experiments on polyamide A at different strain during tensile test and at 60°C.

Strain (%)	1 st craze family						2 nd craze family					
	D _{min} nm	D _{max} nm	L _{min} nm	L _{max} nm	Φ_2	N ₂ mm ⁻³	DD _{min} nm	DD _{max} nm	LL _{min} nm	LL _{max} nm	Φ_2'	N' ₂ mm ⁻³
9%	5	20	1	10	3.0×10^{-6}	9.0×10^{10}	50	150	30	90	9.0×10^{-6}	4.5×10^6
20%	5	50	2	50	2.8×10^{-6}	3.7×10^9	100	1300	40	300	4.8×10^{-4}	3.7×10^7
25%	5	50	2	50	8.3×10^{-6}	1.1×10^{10}	100	1500	40	300	1.8×10^{-4}	2.1×10^7
30%	5	50	2	50	2.8×10^{-6}	3.7×10^9	120	1500	40	350	5.3×10^{-4}	6.3×10^7
50%	5	50	2	50	8.3×10^{-6}	1.1×10^{10}	120	1500	40	350	1.8×10^{-4}	2.1×10^7
60%	5	50	2	50	1.4×10^{-5}	1.8×10^{10}	120	1500	35	400	1.7×10^{-4}	2.6×10^7

Table 7 Sizes and volume fractions of damage corresponding to fitting parameters used at different strain for polyamide A at T=60°C in Figure 12 (a-b). N₂ and Φ_2 are the number per unit volume and the volume fraction of the first family of crazes. N'₂ and Φ_2' are the number per unit volume and the volume fraction of the second family of crazes.

The analysis of USAXS results permits to access to the number of the nucleated crazes per unit volume (N₂). Note that the non-monotonous evolution of N₂ may be attributed to the fact that the samples are different for each measurements made on different deformation. At 20% of true strain, 3.7×10^9 of small crazes per unit volume (mm⁻³) have nucleated. The number of pre-existing defects N_i is 1.1×10^9 mm⁻³ as given in Table 6. The number of the small nucleated crazes is of the same order of magnitude as the pre-existing defects. At 60% of true strain, this number is 1.8×10^{10} , which shows that this population of crazes increases slowly in the range of accessible deformation. The initial growth after nucleation of these small crazes is blocked at a size of 100 nm in length. Charvet et al attributed this behavior to the strain hardening which blocks the growth of cavities in this regime of deformation²⁷. Between 9% and 60% of true strain, the size of crazes increases from 40 to 100 nm in length (D_{max}) and from 20 to 100 nm in thickness (L_{max}). Their volume fraction ϕ_2 increases with deformation, from 2.0×10^{-6} to 1.4×10^{-5} . All the values determined for polyamide A at 60°C are reported in Table 7.

Additionally to this first craze family, whose size is limited to 100 nm, we observe a second family of crazes which sizes are larger. This second family is visible at low q values and corresponds to large crazes

with dimensions DD and LL (Table 7). A small fraction of the crazes formed by nucleation of cavities in the vicinity of pre-existing impurities during the first regime grow faster. We denote this small fraction of crazes as “the second family of crazes”. The crazes belonging to the second family are the same type of defects as those of the 1st family but the crazes of the second family are larger. Both correspond to type (2) defects as defined by Figure 6. Crazes of the second family correspond to a minority of crazes which initiate from crazes of the first family but undergo a fast growth process by nucleation in the vicinity of their tip.

As reported in Table 7, there are about 10^7 mm^{-3} (N_2') crazes of the second family, which represents a small fraction of the total number of crazes present in the sample (around 1.0×10^9). The maximum sizes of these crazes are 3000 nm in length (DD_{max}) and 800 nm in thickness (LL_{max}), with a volume fraction of 1.7×10^{-4} . Their growth is blocked at this size.

3.5.3.2 Damaging behavior under tensile deformation of polyamides B and C

Figure 13 shows both parallel and perpendicular scattered intensities at different strain levels at 60°C (a-b) for polyamide B and at 130°C (c-d) for polyamide C. The study of the damage is done in the ductile regime, as explained in 3.1. For both polymers, no evolution of the scattered intensities is observed by USAXS experiments, as observed in Figure 13. At large q values, the curves in both parallel and perpendicular direction overlap (the signal is isotropic). At small q values, the curves do not overlap perfectly, they are not monotonous. This is due to reproducibility, and cavities related to the injection process (each time, a different sample is stretched). We deduce that these polymers do not get damaged up to 50 % of true strain for both polyamide B and polyamide C. We measured only the signal due to cavities related to the injection process.

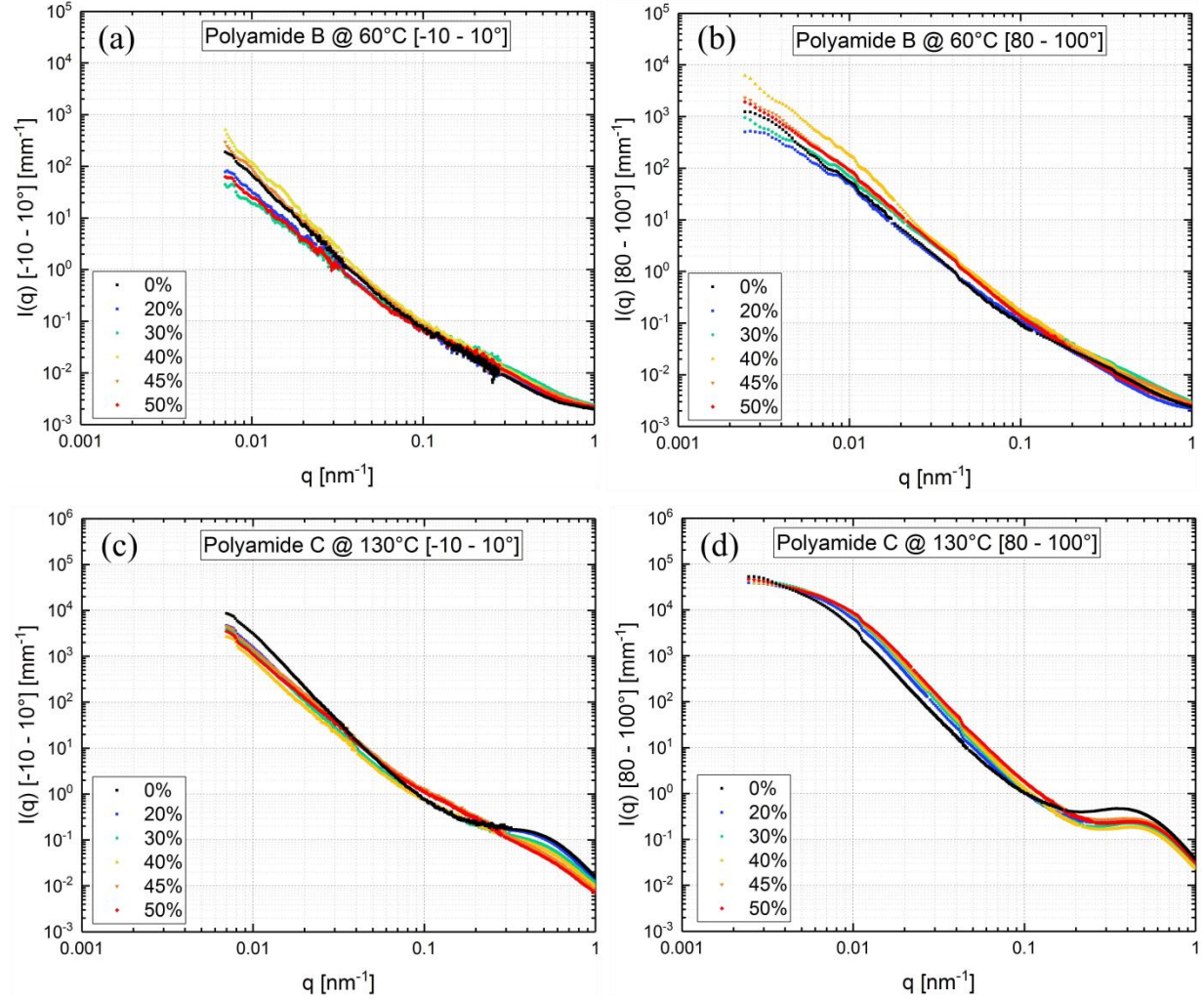


Figure 13 Restricted scattered intensities in the parallel direction (a-c) and perpendicular direction (b-d) to the tensile direction obtained by USAXS experiments on Polyamide B at 60°C (a-b) and Polyamide C at 130°C (c-d) at different strain during tensile test.

3.5.3.3 Behavior under tensile deformation of polycarbonate

Polycarbonate is a tough and ductile polymer at 23°C and for all the considered studied temperatures. Figure 14 shows the restricted scattered intensities in the parallel direction (a) and perpendicular direction (b) to the tensile direction obtained by USAXS experiments on polycarbonate at different strain during tensile test until failure and at 23°C. Experimental data are fitted by global scattered intensity given by

Equations 19 and 20. Thanks to the analysis of the experimental data, the size and the volume fraction of each typology of damage can be determined. All the adjustable parameters are given in Table 8.

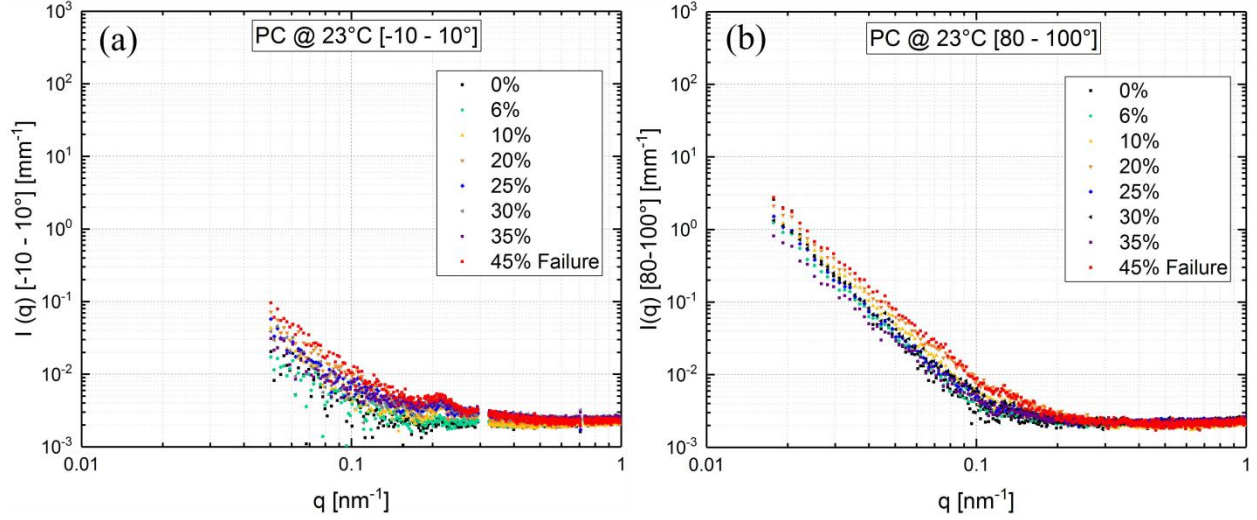


Figure 14 Restricted scattered intensities in the parallel direction (a) and perpendicular direction (b) to the tensile direction obtained by USAXS experiments on polycarbonate at different strain during tensile test until failure at 23°C.

Strain (%)	1 st craze family						2 nd craze family					
	D _{min} nm	D _{max} nm	L _{min} nm	L _{max} nm	Φ ₂	N ₂ mm ⁻³	DD _{min} nm	DD _{max} nm	LL _{min} nm	LL _{max} nm	Φ ₂ '	N ₂ ' mm ⁻³
6%	1	10	1	15	2.6×10 ⁻⁶	1.5×10 ¹⁰	N/A					
10%	1	10	1	15	3.3×10 ⁻⁶	1.8×10 ¹⁰						
20%	1	10	1	15	8.9×10 ⁻⁶	3.2×10 ¹⁰						
25%	1	15	1	15	1.9×10 ⁻⁵	8.8×10 ¹⁰	50	200	80	150	1.3×10 ⁻⁶	2.6×10 ⁵
30%	1	15	1	15	2.0×10 ⁻⁵	8.8×10 ¹⁰	50	300	80	150	1.7×10 ⁻⁶	2.6×10 ⁵
35%	1	15	1	15	2.0×10 ⁻⁵	8.5×10 ¹⁰	50	400	80	150	2.2×10 ⁻⁶	2.6×10 ⁵
45%	1	15	1	20	2.0×10 ⁻⁵	8.2×10 ¹⁰	50	600	80	150	3.1×10 ⁻⁵	2.6×10 ⁵

Table 8 Sizes and volume fractions of damage corresponding to fitting parameters used for polycarbonate at 23°C at different strain until failure in Figure 14. N₂ and Φ₂ are the number per unit volume and the volume fraction of the first family of crazes. N₂' and Φ₂' are the number per unit volume and the volume fraction of the second family of crazes.

In figure 14, we observe a monotonous evolution. Note that by superimposing the curve in both parallel and perpendicular directions, we observe that the diffusion in the parallel direction is slightly higher than in the perpendicular direction. The curves do not overlap. For small cavities (1st family), the difference is not significant (see Table 8). Regarding the large cavities (2nd family) which dominate the scattering at low q , we observe that they are oriented in the direction perpendicular to the traction.

Two size distributions are necessary to describe the contribution of crazes at deformations larger than 25%. At small q values, both the scattered intensities parallel and perpendicular to the tensile direction increase with deformation. This evolution corresponds to the growth of elongated cavities oriented in the direction perpendicular to the tensile direction.

The damage mechanisms of polycarbonate during tensile deformation at 23°C can be defined by two regimes. The first regime is observable at high q values. In this regime, damages are initiated by the nucleation of small crazes, which occurs before 6% of true strain, as visible on Figure 14. These nucleated crazes remain small, with a maximal size of 30 nm in length (Table 8). The volume fraction of these crazes increases with deformation, from 2.6×10^{-6} at 6% of deformation to 2.0×10^{-5} at 45% of deformation. The number of the nucleated crazes per unit volume (N_2) can be determined. At 25% of true strain, 8.8×10^{10} of small crazes per unit volume (mm^{-3}) have nucleated. The number of pre-existing cavities N_1 resulting from the injection process is $3.9 \times 10^5 \text{ mm}^{-3}$ (Table 6). The number of the small nucleated cavities is higher than the pre-existing ones. This number remains constant after 6% of deformation which indicates that these crazes nucleate on impurities. At 45% of true strain (failure of the specimen), this number is still 8.2×10^{10} . The initial growth after nucleation of these small crazes is blocked at a size of 30 nm in length, an effect attributed to strain hardening by Charvet et al²⁷. Between 6% and 45% of true strain, the size of crazes increases from 20 to 30 nm in length (D_{max}) and from 30 to 40 nm in thickness (L_{max}). Their volume fraction ϕ_2 increases with deformation, from 2.6×10^{-6} to 2.0×10^{-5} . All the values determined for polycarbonate at 23°C are reported in Table 8. Note that ϕ_2 is dominated by the lower bound of the integral (small size, D_{min} and L_{min}).

Increasing the strain beyond 25% leads to a new growth regime for a small fraction of the nucleated crazes. This second growth regime is observable at low q values and corresponds to large crazes with dimensions DD and LL (Table 8). A small fraction of the crazes formed by nucleation of cavities on impurities grow faster. As reported in Table 8, the number of these large crazes per unit volume is of order 10^5 mm^{-3} (N_2'), which is much less than the total number of crazes present in the sample (around 8.0×10^{10}). The crazes observed continue to grow until the failure of the specimen at 45% of true strain. At failure, the maximum sizes of these crazes are 1200 nm in length (DD_{max}) and 300 nm in thickness (LL_{max}), with a volume fraction of 3.1×10^{-5} .

3.5.3.4 Behavior under tensile deformation of PMMA

Below 80°C, PMMA is fragile. Above 80°C, PMMA is ductile. Figure 15 shows the restricted scattered intensities in the parallel direction (a) and perpendicular direction (b) to the tensile direction obtained by USAXS experiments on PMMA at different strain during tensile test until failure at 80°C. All the adjustable parameters are given in Table 9. Two size distributions are necessary to describe the contribution of crazes. A bump is visible on the scattered intensity in the direction parallel to the tensile direction (Figure 15-a).

The damage mechanisms of PMMA during tensile deformation at 80°C can be defined by two regimes. The first regime is visible at high q values. In this regime, damages are initiated by the nucleation of small crazes, occurring before 3% of true strain, as visible on Figure 15. These nucleated crazes remain small, with a maximal size of 200 nm in length (Table 9). The volume fraction of these crazes increases with deformation, from 2.0×10^{-5} to 1.5×10^{-4} .

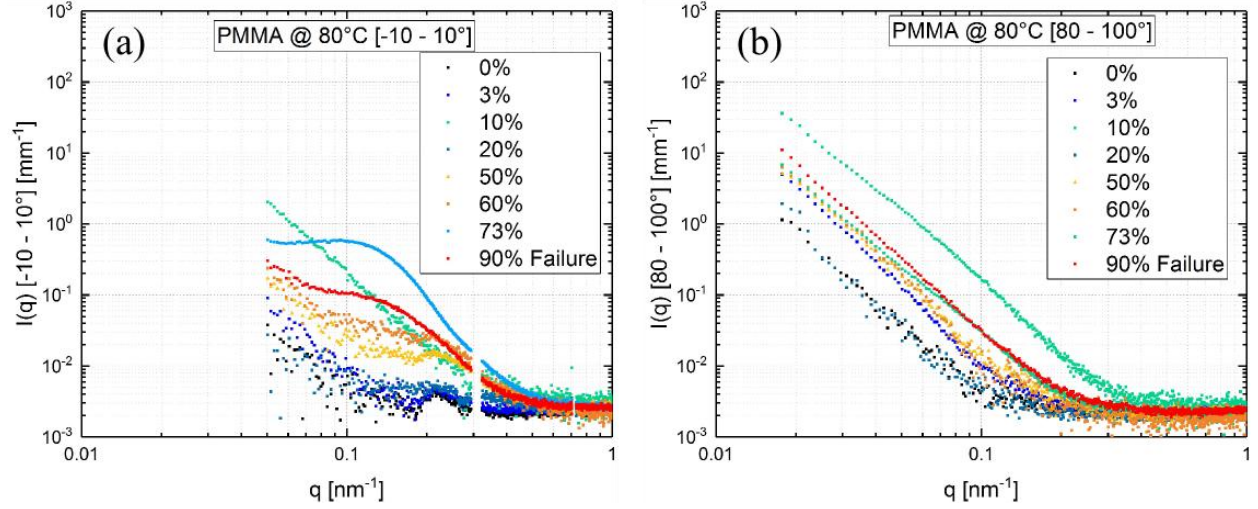


Figure 15 Restricted scattered intensities in the parallel direction (a) and perpendicular direction (b) to the tensile direction obtained by USAXS experiments on PMMA at different strain during tensile test until failure at 80°C.

Strain (%)	1 st craze family						2 nd craze family					
	D _{min} nm	D _{max} nm	L _{min} nm	L _{max} nm	Φ_2	N ₂ mm ⁻³	DD _{mi} nm	DD _{max} nm	LL _{min} nm	LL _{max} Nm	Φ_2'	N _{2'} mm ⁻³
3%	1	70	1	20	2.0×10^{-5}	2.7×10^8						
10%	1	70	1	20	4.3×10^{-5}	2.8×10^8					N/A	
20%	1	70	1	20	5.2×10^{-5}	2.8×10^8						
50%	1	70	1	20	2.0×10^{-5}	2.7×10^8	50	200	30	100	8.3×10^{-6}	2.4×10^4
60%	1	70	1	20	2.0×10^{-5}	2.7×10^8	50	250	30	100	2.1×10^{-5}	2.3×10^4
73%	1	80	1	30	1.5×10^{-4}	2.6×10^8	50	300	30	100	1.8×10^{-5}	2.4×10^4

Table 9 Sizes and volume fractions of damage corresponding to fitting parameters used at different strain for PMMA at 80°C in Figure 15. N₂ and Φ_2 are the number per unit volume and the volume fraction of the first family of crazes. N_{2'} and Φ_2' are the number per unit volume and the volume fraction of the second family of crazes.

The number of the nucleated crazes per unit volume (N₂) can be determined. At 3% of true strain, the number of small crazes per unit volume is of order $2.7 \times 10^8 \text{ mm}^{-3}$. This number remains constant almost up to failure. All the impurities present do not lead to nucleation on injection, but they can do so under deformation. When the number of cavities is constant, it is a sign of heterogeneous nucleation. It is also

the case for polycarbonate. The number of pre-existing cavities N_i is $4.2 \times 10^7 \text{ mm}^{-3}$ (Table 6). The number of the small nucleated crazes is higher than the pre-existing cavities. The initial growth after nucleation of these small crazes is blocked at a size of 160 nm in length, which we assume is due to strain hardening²⁷. The size of crazes slowly increases with the deformation until 73% of deformation, from 140 to 160 nm in length. Their volume fraction ϕ_2 increases with deformation, from 2.0×10^{-5} to 1.5×10^{-4} . All the values determined for PMMA at 90°C are reported in Table 9. The intensity measured at rupture (90% of true strain) is difficult to interpret. We therefore restrict our discussion at 73% of true strain.

Increasing the strain beyond 50% leads to a new growth regime for a small fraction of crazes. This second growth regime is visible at low q values and corresponds to large crazes with dimensions DD and LL (Table 9). A small fraction of the crazes formed by nucleation of cavities in the vicinity of pre-existing impurities during the first regime grow faster. As reported in Table 9, around 2.10^4 mm^{-3} crazes per unit volume (N_2') are in this second craze family, which is a very small number as compared to the total number of crazes present in the sample (around 1.0×10^{10} per mm^3). The crazes observed continue to grow until 73% of true strain. The maximum sizes of these crazes are 600 nm in length (DD_{max}) and 200 nm in thickness (LL_{max}), with a volume fraction of 1.8×10^{-5} .

4 Interpretation and Discussion

4.1 Introduction

After having described the damaging mechanisms observed by USAXS experiments for the five polymers, we propose to classify these different mechanisms. Charvet et al²⁷ have shown in plasticized cellulose acetate polymers that damage mechanisms under tensile deformation take place in two main stages. Damages are initiated by cavitation. Charvet et al have observed the nucleation of cavities within

the time resolution of the experiment around impurities due to the injection process. These cavities are observed when their sizes have reached a size of order $\xi \approx 50$ or 100 nm. Then, a slow growth regime is observed upon increasing the stress further with a diameter which grows linearly with the stress. The authors propose to explain this moderate growth by the presence of strain hardening. Indeed, tensile experiments on plasticized cellulose acetate polymers display an important strain hardening regime above 8% of true strain⁶⁰. Once a cavity nucleates, the tensile stress around it relaxes. Under the effect of the macroscopic stress the cavity starts to grow and tangential stress increases. At some point, the stress in the vicinity of the cavities becomes sufficiently high to equilibrate the stress on larger scale and the growth is blocked. This effect is the consequence of the strain hardening. Note that without this effect the nucleation of a single cavity in amorphous polymers would lead to rapid breaking of the sample. The same effect is observed with polyamide A, PMMA and polycarbonate.

Cavitation occurs when the isotropic component of the stress in the material (the negative pressure, Π) exceeds a critical value. The critical diameter a_c for cavitation is given by²⁷:

$$a_c = \frac{4\gamma_s}{\Pi} \quad (21)$$

where γ_s the surface tension of the material. Beyond this value a_c , a cavity is unstable and grows rapidly^{61–64} until its growth is blocked by the strain hardening which develops in its vicinity. a_c is of order 1 nm^{61,63,64}.

The corresponding free energy barrier for homogeneous nucleation is given by the following equation:

$$\zeta_{hom}^*(p) = \frac{16\pi\gamma_s^3}{3\Pi^2} \quad (22)$$

Note that in the case of heterogeneous nucleation, the value of the free energy barrier can be reduced by several orders of magnitude. This is the case of CDA²⁷ and also with the polymers considered in this manuscript.

Figure 16 gives a schematic representation of the first regime of craze growth, where Π is the macroscopic imposed stress, σ_{tan} is the local stress in the equator position of the cavity, $a(0)$ is the initial cavity diameter and R is the final diameter that the cavity can reach. When the cavity grows, the tangential stress increases.

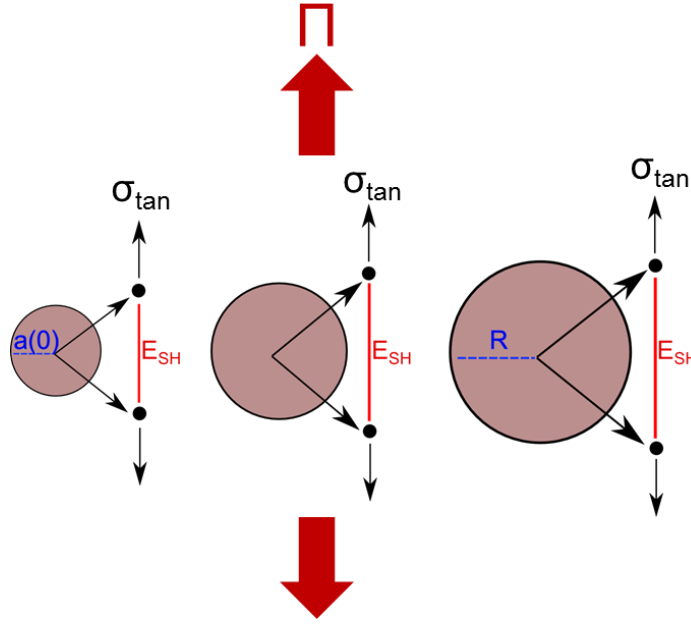


Figure 16 Representation of the first regime of craze growth, blocked by the strain hardening regime.

The size R at which the strain hardening blocks the growth of the cavity is given by:

$$R = \kappa \frac{\Pi}{E_{SH}} a(0) + a(0) \quad (23)$$

Where κ is a number of order 1, $a(0)$ is an initial effective cavity diameter corresponding to the distance from a free interface beyond which the polymer recovers its bulk properties^{27,65–67}. E_{SH} is the strain hardening modulus. From Equation (23), one can deduce indeed that the growth of the cavities in this regime is linear with the applied stress and that this growth does not stem from new damages but is purely elastic and plastic in nature.

Once the applied stress becomes sufficiently high, the growth of the cavities enters a new regime. A small fraction of these crazes start to grow faster until the failure of the sample. Charvet et al propose that this growth is governed by a mechanism of successive homogeneous nucleations of new cavities in the vicinity of the existing cavities, just ahead of them where the stress is the largest. Indeed, when a craze reaches a sufficiently large size, or when the local stress level is sufficiently high, this craze becomes unstable and propagates as a crack resulting in the failure of the sample. Figure 17 gives a schematic representation of this mechanism.

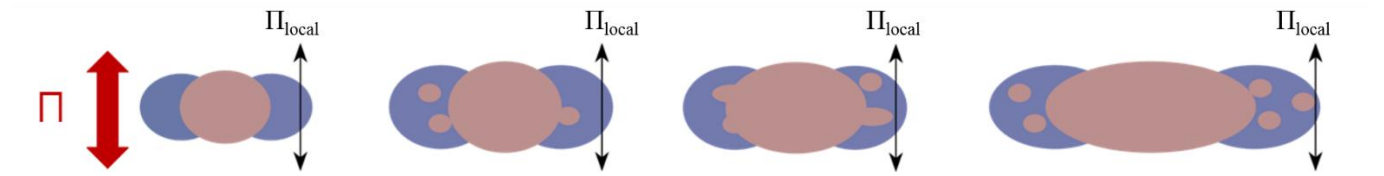


Figure 17 Schematic representation of the growth crazes by nucleation of cavities followed by a coalescence mechanism.

The breaking time t_{∞} starting from a craze of size of $D(0)$ is found to be²⁷ :

$$t_{\infty} \approx \frac{a_c^3}{\xi D^2(0)} \tau \quad (24)$$

If we consider that the nucleation time τ is of order $\tau_r = 10^8$ s, $a_c \sim 1$ nm; $\xi \sim 100$ nm and $D(0) \sim 100$ nm, the sample breaks in a time $t_{\infty} \approx 100$ s which corresponds to the order of magnitude of the experimental time scale.

This regime is unstable. The nucleation time τ decreases sharply when the stress increases. The evolution of the nucleation time as a function of the applied stress is given by equation:

$$\ln\left(\frac{\tau}{\tau_r}\right) \approx \ln\left(\frac{\tau_r}{\tau_0}\right) \left[\frac{\Pi_r^2}{\Pi^2} - 1 \right] \approx 46 \left[\frac{\Pi_r^2}{\Pi^2} - 1 \right] \quad (25)$$

With Π the local stress, $\tau_r = 10^8$ s, Π_r is the local stress at breaking.

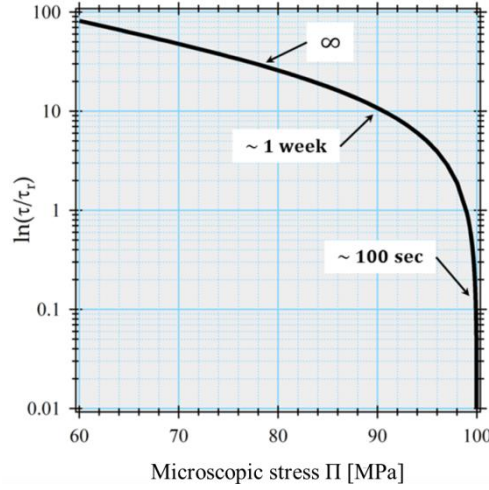


Figure 18 Evolution of $\ln(\tau/\tau_r)$ as a function of the microscopic stress Π . From Charvet et al²⁷.

Figure 18 shows the instability of this regime. Indeed, the rupture time is highly sensitive to the stress. If we assume as in Charvet et al study²⁷ that the local stress corresponding to rupture of the material in the experimental time scale is 100 MPa (for the sake of being specific), the nucleation time is $\tau_r = 10^8$ s and the corresponding macroscopic breaking time is $t_\infty \sim 100$ s. If the local stress is decreased to 85 MPa, the macroscopic breaking time is $t_\infty \sim 10^{10}$ s, which can be considered infinite for all practical purposes. The breaking time is thus strongly non-linear as a function of the applied macroscopic stress.

Our study focuses on five polymers, three of which do not break (the three PPA) and among them two of which are not damaged at all during deformation (polyamide B and C). The analysis of these different polymers by USAXS highlights different modes of ultimate behavior and damaging which we discuss now. The three PPA display a stabilized necking in the strain hardening regime and do not break, while the polycarbonate and PMMA do not show necking and deform homogeneously. The latter break at some point in the strain hardening regime. It can be observed that polyamide A has a stabilized damage and do not break, which is not the case for polycarbonate and PMMA, which have unstabilized damage and break in a way similar to that of cellulose acetate⁶⁰.

4.2 *Damage mechanisms of polycarbonate and PMMA*

The studied polycarbonate and PMMA have a behavior similar to another amorphous ductile polymer, the plasticized cellulose acetate studied by Charvet et al²⁷. Unlike the studied PPA, these two polymers deform homogeneously without necking as it is the case of the CDA studied by Charvet et al. The damage mechanism can be described by a two-steps mechanism for both polycarbonate and PMMA, and is the same as the mechanism described by Charvet et al for plasticized cellulose acetate⁶⁰.

For PMMA at 80°C, during the first step, USAXS analysis show that small crazes with a size comprised between 2 and 160 nm nucleate simultaneously within the time resolution of our experiment, before 3 % of true strain. The number of these nucleated crazes per unit volume is found to be of order $N_2 = 2.7 \times 10^8 \text{ mm}^{-3}$, which is the same order of magnitude as but larger than that of the number of cavities initially present in the sample (which result from the injection process) with $N_i = 4.2 \times 10^7 \text{ mm}^{-3}$, measured on samples before tensile testing, as reported in Table 6. After this initial stage, it is observed that the number of nucleated crazes no longer varies with the deformation until 73% of deformation. The small increase of the volume fraction ϕ_2 and the size of these crazes with the deformation indicate that these initial crazes nucleation is followed by a slow craze growth without new nucleation, with a size which increases linearly with the stress according to Equation 23, as reported in Table 9. At 3% of true strain, PMMA displays a volume fraction of crazes $\phi_2 = 2.0 \times 10^{-5}$ with a maximum length of 140 nm. With polyamide 6,6 which is a semi-crystalline polymer, Mourglia-Seignobos et al have shown that the craze growth is blocked by the crystalline phase⁴⁹. PMMA is amorphous. In absence of a crystalline phase, the crazes growth should lead to a rapid brittle failure soon after the appearance of a single cavity after 3% of deformation. This is not what is observed. According to Charvet et al's work, we interpret the ductility observed in PMMA as a consequence of the strain hardening which blocks the propagation of crazes, as it is the case of cellulose acetate.

A 2nd family of crazes is observed at 50% of true strain for PMMA, which corresponds to a macroscopic stress of about 18 MPa. The number of crazes per unit volume is of order $N_2' = 2.4 \times 10^4 \text{ mm}^{-3}$, as shown in Table 9. The small volume fraction of observed crazes, even after failure, indicates that this second craze family cannot result from a mechanism of crazes coalescence. This second family of larger crazes corresponds to a very small proportion of crazes initially nucleated (1st regime) which grow faster than the rest of the initial crazes population as a consequence of the strong instability discussed in section 4.1, Figure 16. Upon increasing the deformation, and when the applied stress becomes sufficiently high, the sample breaks due to crack propagation.

In the case of polycarbonate at 23°C, USAXS analysis shows that small crazes with a size comprised between 2 and 20 nm nucleate simultaneously within the time resolution of our experiment, before 6% of true strain. The number of these nucleated crazes per unit volume is found to be of order $N_2 = 1.5 \times 10^{10} \text{ mm}^{-3}$, which is higher than the number of cavities initially present in the sample with $N_i = 3.9 \times 10^5 \text{ mm}^{-3}$ (as reported in Table 6) and which result from the injection process. It is observed that the number of nucleated crazes increases until 25% of deformation, but no longer varies afterwards until failure at 45% and reaches a value $N_2 = 8.2 \times 10^{10} \text{ mm}^{-3}$. The small increase of the volume fraction ϕ_2 and of the size of these crazes with the deformation indicates that this initial crazes nucleation is followed by a slow craze growth without new nucleation, as reported in Table 8. At 6% of true strain, polycarbonate has a volume fraction of crazes $\phi_2 = 2.6 \times 10^{-6}$ with a maximum length of 20 nm. As in PMMA, there is no crystalline phase in polycarbonate which is amorphous. In absence of this crystalline phase which blocks the propagation of crazes in PA66 for instance, the crazes growth would lead to a rapid brittle failure soon after the appearance of a single cavity after 6% of deformation. This is not what is observed. Here also, we interpret this fact as a consequence of the strain hardening which blocks the propagation of crazes.

When the applied stress is sufficiently high, the sample breaks due to a crack propagation. A 2nd family of large crazes is observed after 25% of true strain, which corresponds to a macroscopic stress of about 45

MPa. The number of these large crazes per unit volume is of order $N_2' = 2.6 \times 10^5 \text{ mm}^{-3}$, as shown in Table 8. The small volume fraction of observed crazes, after failure indicates that this second craze family cannot result from a mechanism of crazes coalescence. This second family of larger crazes which reach a size of 600 nm at 45% of deformation results from a very small proportion of crazes initially nucleated (1st regime) which grow faster than the rest of the initial crazes population as a consequence of the instability mechanisms discussed in section 4.1.

As we shall see in the case of polyamide A, two mechanisms can prevent nucleation from occurring: the reduction of the volume variation under applied strain, and the increase of the surface tension of the polymer γ_s in the strain hardening regime. We do observe an increase of surface tension by 15% and 33% for PMMA and polycarbonate, respectively. This effect appears to be insufficient to prevent cavitation. Note that the volume increase by 5% and 10% at break for PMMA and polycarbonate respectively. This increase may be thought as favoring cavitation.

As it is the case for PMMA, the damaging behavior until breaking of polycarbonate is the same as that of cellulose acetate²⁷.

4.3 *Damage mechanisms of polyphthalamides*

Let us consider the case of the three PPA. None of them break, contrarily to the case of the plasticized cellulose acetate studied by Charvet et al or that of polycarbonate and PMMA studied here. Two of these PPA do not display damaging at all (polyamides B and C). Polyamide A gets damaged but do not break.

4.3.1 Polyamide A

In the case of polyamide A, necking appears at 5% of true strain. We observe two families of crazes at 9% of deformation. The number of crazes does not evolve with the deformation and their size is about 20 nm. They represent a volume fraction of 3.0×10^{-6} . The second family of crazes which represents a volume

fraction of 9.0×10^{-6} at 9% of deformation has a size of 150 nm. Craze nucleation occurs thus before 9% of deformation. Upon increasing the stress further, we observe that the size of the first family grows roughly linearly with the stress from 20 nm to 50 nm. The size of the crazes of the second family increases from 150 nm to 1500 nm. However, at odds with the case of CDA, these large crazes do not lead to breaking at least within the accessible deformation range of our apparatus. The growth of these large crazes is stopped at a few microns, just after the yielding. This effect is not observed with the CDA studied by Charvet et al²⁷.

Our interpretation is that cavitation is suppressed after the yielding for polyamide A. Therefore, no new cavities can appear and the already existing cavities cannot grow further. Two mechanisms can prevent nucleation from occurring: the reduction of the volume variation and the increase of the surface tension of the polymer γ_s . Indeed, the necking process is accompanied by a decrease in volume variation, which may contribute to the suppression of cavitation. In the case of polyamide A, the volume increases until the yielding, and then remains constant, as observed in Figure 4-a. We have calculated the Poisson's ratio ν of polyamide A, and we find a Poisson's ratio less than 0.5 before necking, and equal to 0.5 just after the beginning of necking, in the strain softening regime and which keeps this value afterwards. In addition, strong molecular cohesion contributes to suppress cavitation. Surface tension is higher in the strain hardening regime for all polymers. For polyamide A after deformation, in the necking zone, the surface tension γ_s increases from 54.8 mJ/m² to 65.5 mJ/m², an increase of almost 20%.

Our interpretation for the observed stabilized damages in polyamide A is that this may be the consequence of two effects: the reduction of the volume variation, which is the consequence of the increase of the Poisson's ratio, and of the surface tension of the polymer in the strain hardening regime. One can see in Figure 4-a that the volume increase under applied strain is suppressed at about 5% of deformation in the case of polyamide A. To the best of our knowledge, no complete model for cavitation exist in solid polymers taking into account the volume variation under uniaxial deformation. However, one may assume that a Poisson ratio close to 0.5 inhibits cavitation in these circumstances, as compared

to triaxial applied stress^{63,64}, as cavitation is considered in liquids. In addition, the increase of surface tension by about 20% in the strain hardening regime (see Table 5) leads to an increase of the free energy barriers by a factor close to 2 according to Equation 22. Both effects tend to suppress cavitation. The growth of the large crazes (and also that of the smaller ones which are blocked at about 50 nm in diameter) is no longer possible. Strain hardening blocks the size of crazes at a few micrometers in the absence of new nucleations ahead of the crazes.

4.3.2 Polyamide B and polyamide C

The third category concerns the two low semi-crystalline PPA, polyamide B and polyamide C. These two semi-crystalline PPA deform by necking, which appears just after the yielding. In the case of these polymers, no damaging takes place at all. No crazes are observed before yield, at yield and in the strain hardening regime. The absence of cavitation in the case of polyamide B and polyamide C can be interpreted macroscopically by the fact that the critical stress required for cavitation, $\sigma_{\text{cavitation}}$, is larger than the yield stress σ_y and remains larger afterwards than the stress in the strain hardening regime. Note that we assume that local strain hardening just ahead of a craze is similar to that observed macroscopically. Another mechanism for the local strain hardening may be crystallization. We studied our samples before and after deformation by WAXS and we did not observe any crystallization. But the volume fraction of crazes is very small and we cannot rule out the possibility of crystallization at the craze tip where the strain amplitude is the largest, as seen in the case of natural rubber⁶⁸.

Cavitation depends on several parameters. It depends on the surface tension γ_s , and on the volume variation during applied strain. Essentially, a polymer is fragile if the second growth regime, during which a fraction of the crazes start to grow by homogeneous nucleation in their immediate vicinity, takes place before yield stress, whereas a polymer may be ductile when this is the reverse and if the strain hardening is strong enough. In our interpretation, it means that a polymer is fragile when the free energy barriers for

homogeneous cavitation are reached at smaller deformations than yield stress. It may be the case for polymers with low surface tension, small Poisson's ratio (large increase of volume) and/or for high yield stress. We assume that that polyamides B and C do not get damaged because the stress for cavitation even in the presence of impurities satisfies to the relation $\sigma_{\text{cavitation}} > \sigma_y$, an effect which may be enhanced by large surface tensions, high Poisson's ratio (close to 0.5), and/or low yield stress. Note that the volume variations for both polymers (Figures 4-b and 4-c) do not allow to conclude unambiguously at this regard. However the large increase of the surface tension (both increase by 28% in the strain hardening regime) and possibly a relatively low yield stress may lead to this behavior where damage does not take place.

4.3.3 Summary of damage mechanisms observed

The different damage mechanisms observed are schematized in Figure 19 and Figure 20. Damage is initiated by the simultaneous nucleation of cavities (sizes of order 50 to 100 nm) around pre-existing impurities. This process is observed for polyamide A, polycarbonate and PMMA. The growth of these cavities just after nucleation is blocked by the local strain hardening of the polymer in the immediate vicinity of these cavities. We assume that this local strain hardening mechanism is the same as that measured macroscopically though we cannot measure it locally. During this regime where the cavities are stabilized by the strain hardening, these cavities grow linearly with the macroscopic stress, without new damages (Figure 19-a-b-c). For polyamide A, the appearance before yield of a second family of large crazes of a few micrometers in length is also observed, but their growth after yield in the stress softening regime is blocked and does not resume in the strain hardening regime.

As a consequence, polyamide A does not break within the accessible range of strain of our tensile machine. In the case of polycarbonate and PMMA (Figure 20), when the applied stress becomes sufficiently high, a small fraction of these cracks become unstable and grow faster by nucleation of new cavities just ahead of them and cause the rupture of the sample. Note that these polymers don't exhibit necking.

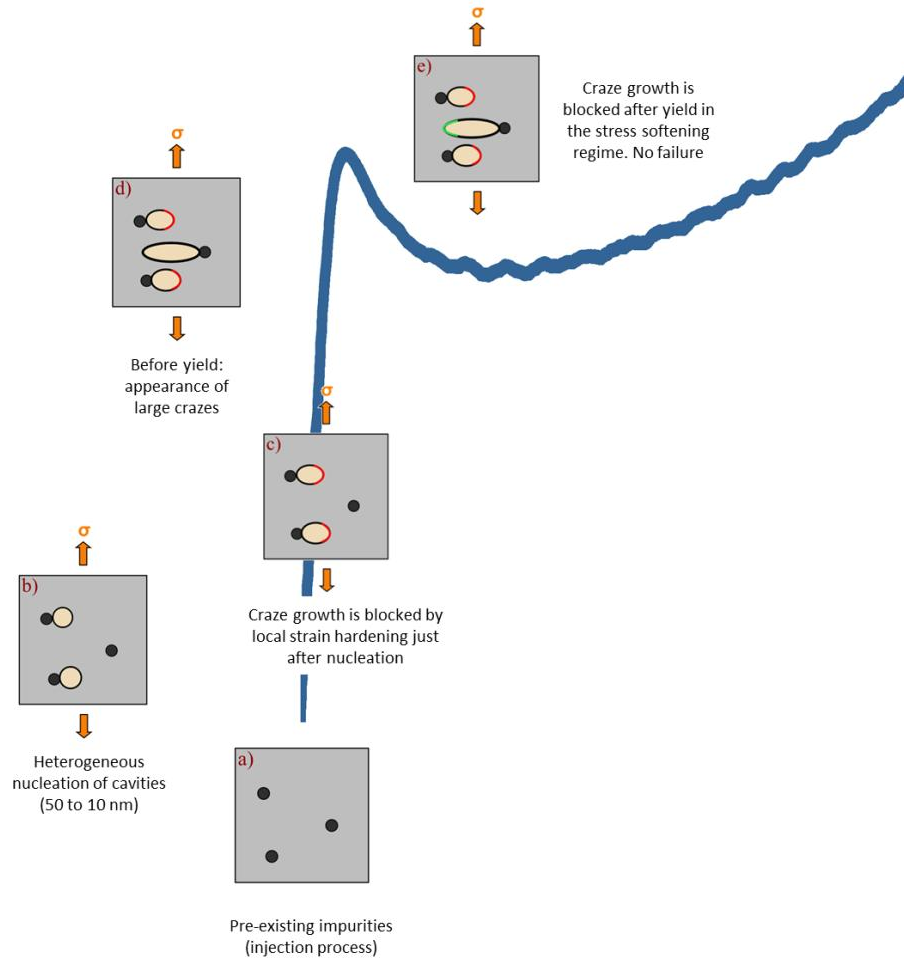


Figure 19 Damage mechanisms of polyamide A under tensile deformation: a) Pre-existing impurities due to the injection process (before tensile experiment), b) Heterogeneous nucleation of cavities, or order 50 to 100 nm, c) The craze growth is blocked by the local strain hardening of the polymer, just after nucleation, in the vicinity of these cavities, d) Appearance before yield of a 2nd family of large crazes and e) Craze growth after yield is blocked in the stress softening regime.

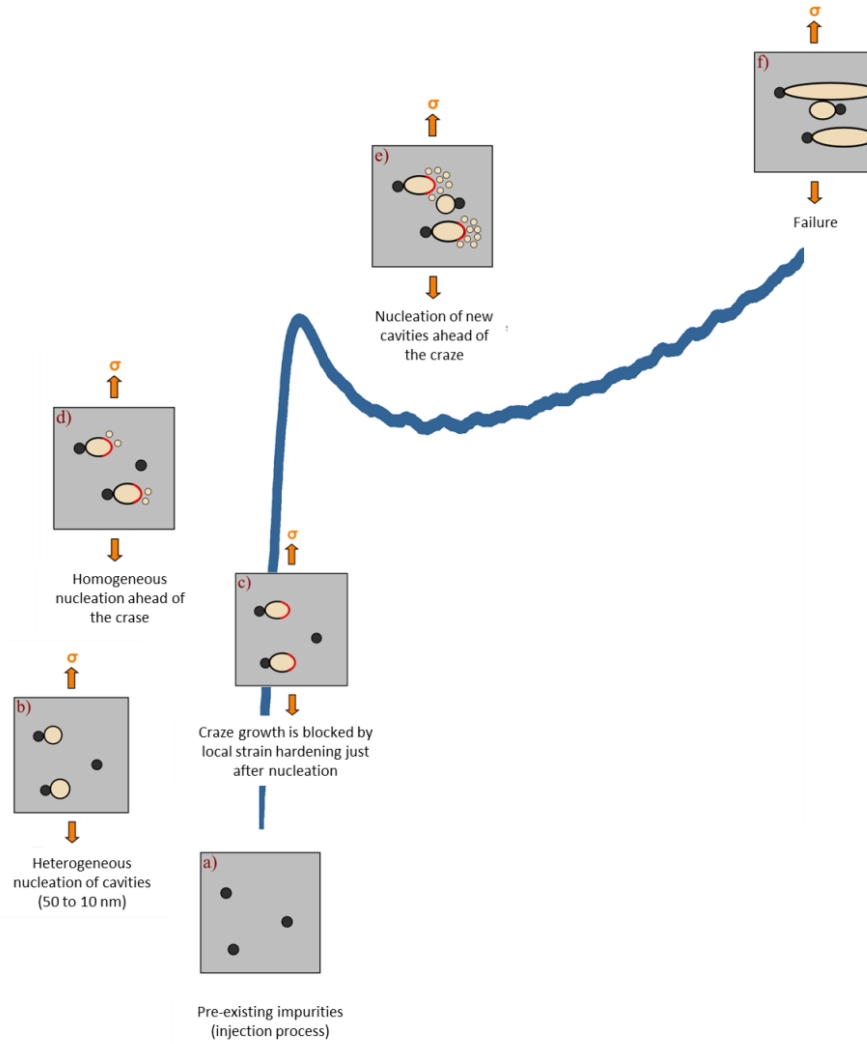


Figure 20 Damage mechanisms of polycarbonate and PMMA under tensile deformation: a) Pre-existing impurities due to the injection process (before tensile experiment), b) Heterogeneous nucleation of cavities, or order 50 to 100 nm, c) The craze growth is blocked by the local strain hardening of the polymer, just after nucleation, in the vicinity of these cavities, d-e) Homogeneous nucleation in the immediate vicinity of the craze, f) Failure of the specimen when a craze reaches a critical growth rate.

5 Conclusion

The analysis of the damaging mechanisms for different polymers (amorphous and semi-crystalline PPA, PC, PMMA) by USAXS highlights different modes of damage for amorphous and low semi-crystalline polymers. Damage, when it occurs, is initiated by the simultaneous nucleation of cavities which grow

rapidly in this stage to reach a size of order 50 to 100 nm around pre-existing impurities due to the injection process. This process is observed for polyamide A, polycarbonate and PMMA, in a mechanism similar to that observed in the case of cellulose acetate²⁷. The growth of these cavities at the end of this rapid growth is blocked by the local strain hardening of the polymer in the immediate vicinity of these cavities, where the strain and the stress are the largest, when this local stress is able to equilibrate the macroscopic stress due to the applied deformation. During the regime where the cavities are stabilized by the strain hardening, these cavities grow linearly with the macroscopic stress, without new damages. In the case of polycarbonate and PMMA, when the applied stress becomes sufficiently high, a small fraction of these cracks become unstable and grow faster by homogeneous nucleation of new cavities just ahead of them which causes the rupture of the sample in a similar way as that observed for cellulose acetate²⁷. This process is identified by the USAXS measurements which show the existence of a small number of large crazes in this regime. In the case of polyamide A we also observe the appearance before the yielding of a second family of large crazes of a few micrometers in length. The second family of crazes are type (2) defects as defined in Figure 6 which undergoes a relatively fast growth process when the local stress is sufficiently high. However, for polyamide A the growth of the second family crazes is suppressed after the yielding and does not resume in the strain hardening regime. As a consequence, polyamide A does not break within the accessible range of strain of our apparatus. This polymer undergoes a stable necking regime, without further damage. This behavior may be the consequence of an increase of the Poisson's ratio after yield and an increase of the surface tension at large deformations. Both effects contribute to a suppression of cavitation. Note that this polymer is ductile above -40°C. Below this temperature, in the fragile regime, the strain hardening regime cannot be reached, and it is expected that the least cavitation may propagate and a brutal rupture may be observed. There will therefore be no intermediate stage where the strain hardening will block the propagation of damage. Indeed, it is difficult to quantify the intermediate stages in the brittle regime, as we observed for PMMA in our experiments. The two semi-crystalline PPA, polyamide B and polyamide C deform by stable necking at large deformation without any damage and do not break. The critical stress for cavitation remains larger than the current stress at

every step of the applied deformation for these two amorphous and low semi-crystalline polymers. Unlike the semi-crystalline polymer studied by Mourglia-Seignobos et al in fatigue ⁴⁹, there is no damage seen in the case of Polyamide C. No specific role of crystallinity was observed as regard to damage in our samples.

The mechanism we propose differs from those proposed by Argon⁶⁹ or by Argon and Hannoosh^{70,71} who ruled out the nucleation of cavities as the elementary process. Based on the work done recently by Charvet et al²⁷ it appears that nucleation is possible on impurities (heterogeneous nucleation) in the initiation stage, and that at higher stress levels homogeneous nucleation is possible indeed just ahead of crazes where stress concentration is the highest. This latter process leads to the growth of a small fraction of crazes and to failure in cellulose acetate, polycarbonate and PMMA. This nucleation process of new cavities just ahead of craze tips is consistent with the apparition of fibrils. Indeed, between neighboring and growing cavities, thin polymer films are formed. Once they reach a thickness of order 10 nm, they become unstable due to disjoining pressure effects and they are expected to rupture⁷². This mechanism should lead to a fibril-like structure. In our experiments, we observed that damage, when it occurs, is initiated by the simultaneous nucleation of cavities (heterogeneous nucleation) which reach rapidly sizes of order 50 to 100 nm, in a similar way as what was observed in the work of Charvet et al²⁷. The number of cavities does not evolve afterwards until breaking. We can assume that the same impurities which allow for the creation of cavities during injection lead also to the cavitation of crazes under applied stress. Their number has been found to be of order 10^{10} mm^{-3} for polyamide A and polycarbonate, and of order 10^8 mm^{-3} for PMMA.

Note that all of our studied polymers exhibit strain hardening which does not seem compatible with the meniscus instability^{40,73} picture used for polymers by Argon and Salama⁴⁰. The nucleation models discussed in this manuscript and by Charvet et al²⁷ explain the strong dependences of the growth rate as a function of the macroscopic applied stress. Indeed, the nonlinear growth kinetics as a function of

both the macroscopic applied stress and the size of cavities can explain why only a small fraction of cavities undergo a second growth step process. In literature, strongly nonlinear constitutive relations are used for describing this nonlinear growth kinetics of the type $\frac{d}{dt}\gamma \propto \sigma^m$, where the exponent m can be equal to or larger than 20^{36,74}. These constitutive relations derive from an Eyring picture⁷⁵. The nucleation mechanism which we propose leads naturally to a strongly non-linear behavior. Note that there is a need to extend the current model for cavitation to deal explicitly with the uniaxial nature of the applied strain, in the presence of solid impurities, or in the vicinity of strain-hardened cavities beyond the current standard cavitation model^{27,63,64}.

Our qualitative interpretation of these effects lead us to propose that the no-damaging mechanism is favored by a high surface tension of the polymer and a relatively low yield stress which prevents cavitation before yield. It is also favored by an increase of the Poisson's ratio after the stress softening regime and an increase of the surface tension of the polymer in this regime. These mechanisms should be the subject of further scientific studies in order to demonstrate them more precisely, beyond the qualitative discussion proposed in this manuscript. In perspective, it would be interesting to modify the chemical structure of polymers, in order to increase molecular cohesion (and therefore increase γ_s)^{76,77}, as well as an enhancement of the strain hardening behavior. As a conclusion, we observe that at least three different damaging behaviors can be observed in the ductile regime of polymers exhibiting strain hardening.

6 References

- (1) Kohan, M. I. *Nylon Plastics Handbook*; Hanser Publishers, 1995.
- (2) Duval, C. Plastiques et automobile - D'hier à aujourd'hui. *Techniques de l'Ingénieur* **2007**, AM 3590-1.
- (3) Duval, C. Plastiques et automobile - D'aujourd'hui à demain. *Techniques de l'Ingénieur* **2007**, AM 3591-1.
- (4) Uddin, A. J.; Ohkoshi, Y.; Gotoh, Y.; Nagura, M.; Endo, R.; Hara, T. Melt Spinning and Laser-Heated Drawing of a New Semiaromatic Polyamide, PA9-T Fiber. *Journal of*

- Polymer Science Part B: Polymer Physics* **2004**, 42, 433–444. <https://doi.org/10.1002/polb.10710>.
- (5) Leboeuf, C.; Harbourn, D. A. Synthesis of Semi-Crystalline Polyphthalamides through Reactive Extrusion of Hexamethylene Terephthalamide Oligomer with Lower Melting, Semi-Crystalline or Amorphous Polyamides. WO1999061509A1, 1999.
 - (6) Novitsky TF; Lange CA; Mathias LJ; Osborn S; Ayotte R; Manning S. Eutectic Melting Behavior of Polyamide 10,T-Co-6,T and 12,T-Co-6,T Copolyterephthalamides. *Polymer* **2010**, 51 (11), 2417–2425. <https://doi.org/10.1016/j.polymer.2010.03.045>.
 - (7) Brandrup, J.; Immergut, E. H.; Grulke, E. A. *Polymer Handbook*, 4th Edition; Wiley, 2003.
 - (8) Govaert, L. E.; Engels, T. A. P.; Wendlandt, M.; Tervoort, T. A.; Suter, U. W. Does the Strain Hardening Modulus of Glassy Polymers Scale with the Flow Stress? *Journal of Polymer Science Part B: Polymer Physics* **2008**, 46 (22), 2475–2481. <https://doi.org/10.1002/polb.21579>.
 - (9) Haward, R. N. Strain Hardening of Thermoplastics. *Macromolecules* **1993**, 26 (22), 5860–5869. <https://doi.org/10.1021/ma00074a006>.
 - (10) Kramer, E. J. Open Questions in the Physics of Deformation of Polymer Glasses. *Journal of Polymer Science Part B: Polymer Physics* **2005**, 43 (23), 3369–3371. <https://doi.org/10.1002/polb.20639>.
 - (11) Arruda, E. M.; Boyce, M. C. Evolution of Plastic Anisotropy in Amorphous Polymers during Finite Straining. *International Journal of Plasticity* **1993**, 9 (6), 697–720. [https://doi.org/10.1016/0749-6419\(93\)90034-N](https://doi.org/10.1016/0749-6419(93)90034-N).
 - (12) Senden, D. J. A.; van Dommelen, J. A. W.; Govaert, L. E. Strain Hardening and Its Relation to Bauschinger Effects in Oriented Polymers. *Journal of Polymer Science Part B: Polymer Physics* **2010**, 48 (13), 1483–1494. <https://doi.org/10.1002/polb.22056>.
 - (13) Jatin; Sudarkodi, V.; Basu, S. Investigations into the Origins of Plastic Flow and Strain Hardening in Amorphous Glassy Polymers. *International Journal of Plasticity* **2014**, 56, 139–155. <https://doi.org/10.1016/j.ijplas.2013.11.007>.
 - (14) Senden, D. J. A.; Krop, S.; van Dommelen, J. A. W.; Govaert, L. E. Rate- and Temperature-Dependent Strain Hardening of Polycarbonate. *Journal of Polymer Science Part B: Polymer Physics* **2012**, 50 (24), 1680–1693. <https://doi.org/10.1002/polb.23165>.
 - (15) Senden, D. D. Strain Hardening and Anisotropy in Solid Polymers. Technische Universiteit Eindhoven 2013. <https://doi.org/10.6100/ir747901>.
 - (16) Hoy, R.; Robbins, M. Strain Hardening of Polymer Glasses: Effect of Entanglement Density, Temperature, and Rate. *Journal of Polymer Science Part B: Polymer Physics* **2006**, 44, 3487–3500. <https://doi.org/10.1002/polb.21012>.
 - (17) Hoy, R.; Robbins, M. Strain Hardening in Polymer Glasses: Limitations of Network Models. *Physical review letters* **2007**, 99, 117801. <https://doi.org/10.1103/PhysRevLett.99.117801>.
 - (18) Hoy, R.; Robbins, M. Strain Hardening of Polymer Glasses: Entanglements, Energetics, and Plasticity. *Physical review. E, Statistical, nonlinear, and soft matter physics* **2008**, 77, 031801. <https://doi.org/10.1103/PhysRevE.77.031801>.
 - (19) Robbins, M. O.; Hoy, R. S. Scaling of the Strain Hardening Modulus of Glassy Polymers with the Flow Stress. *Journal of Polymer Science Part B: Polymer Physics* **2009**, 47 (14), 1406–1411. <https://doi.org/10.1002/polb.21734>.

- (20) Wendlandt, M.; Tervoort, T. A.; Suter, U. W. Strain-Hardening Modulus of Cross-Linked Glassy Poly(Methyl Methacrylate). *Journal of Polymer Science Part B: Polymer Physics* **2010**, *48* (13), 1464–1472. <https://doi.org/10.1002/polb.21979>.
- (21) Millot, C. Multi-Scale Characterization of Deformation Mechanisms of Bulk Polyamide 6 under Tensile Stretching below and above the Glass Transition. PhD Thesis, INSA de Lyon, 2015.
- (22) G'sell, C.; Hiver, J. M.; Dahoun, A. Experimental Characterization of Deformation Damage in Solid Polymers under Tension, and Its Interrelation with Necking. *International Journal of solids and structures* **2002**, *39* (13–14), 3857–3872.
- (23) Ponçot, M.; Addiego, F.; Dahoun, A. True Intrinsic Mechanical Behaviour of Semi-Crystalline and Amorphous Polymers: Influences of Volume Deformation and Cavities Shape. *International Journal of Plasticity* **2013**, *40*, 126–139. <https://doi.org/10.1016/j.ijplas.2012.07.007>.
- (24) Kierkels, JTA (Jules). Tailoring the Mechanical Properties of Amorphous Polymers. Technische Universiteit Eindhoven 2006. <https://doi.org/10.6100/ir613293>.
- (25) Melick, H. G. H. van; Govaert, L. E.; Meijer, H. E. H. On the Origin of Strain Hardening in Glassy Polymers. *Polymer* **2003**, *44* (8), 2493–2502. [https://doi.org/10.1016/S0032-3861\(03\)00112-5](https://doi.org/10.1016/S0032-3861(03)00112-5).
- (26) Richeton, J.; Ahzi, S.; Daridon, L.; Rémond, Y. A Formulation of the Cooperative Model for the Yield Stress of Amorphous Polymers for a Wide Range of Strain Rates and Temperatures. *Polymer* **2005**, *46* (16), 6035–6043. <https://doi.org/10.1016/j.polymer.2005.05.079>.
- (27) Charvet, A.; Vergelati, C.; Sotta, P.; Long, D. R. Damage Mechanisms of Plasticized Cellulose Acetate under Tensile Deformation Studied by Ultrasmall-Angle X-Ray Scattering. *Macromolecules* **2019**, *52* (17), 6613–6632. <https://doi.org/10.1021/acs.macromol.9b00858>.
- (28) Meijer, H. E. H.; Govaert, L. E. Mechanical Performance of Polymer Systems: The Relation between Structure and Properties. *Prog. Polym. Sci.* **2005**, *30*, 915–938. *Progress in Polymer Science* **2005**, *30*, 915–938. <https://doi.org/10.1016/j.progpolymsci.2005.06.009>.
- (29) Govaert, L. E.; Tervoort, T. A. Strain Hardening of Polycarbonate in the Glassy State: Influence of Temperature and Molecular Weight. *Journal of Polymer Science Part B: Polymer Physics* **2004**, *42* (11), 2041–2049. <https://doi.org/10.1002/polb.20095>.
- (30) Michler, G. H. Electron Microscopic Investigations of the Structure of Crazes in Polystyrene. *Colloid & Polymer Science* **1985**, *263* (6), 462–474. <https://doi.org/10.1007/BF01458336>.
- (31) Michler, G. H. Crazes in Amorphous Polymers I. Variety of the Structure of Crazes and Classification of Different Types of Crazes. *Colloid & Polymer Science* **1989**, *267* (5), 377–388. <https://doi.org/10.1007/BF01410182>.
- (32) Michler, G. H. Correlation between Craze Formation and Mechanical Behaviour of Amorphous Polymers. *Journal of Materials Science* **1990**, *25* (5), 2321–2334. <https://doi.org/10.1007/BF00638022>.
- (33) García Gutiérrez, M. C.; Michler, G. H.; Henning, S.; Schade, C. Micromechanical Behavior of Branched Polystyrene as Revealed by in Situ Transmission Electron Microscopy and Microhardness. *Journal of Macromolecular Science, Part B* **2001**, *40* (5), 797–812. <https://doi.org/10.1081/MB-100107562>.

- (34) Michler, G. H. *Electron Microscopy of Polymers*; Springer Laboratory; Springer Berlin Heidelberg, 2008.
- (35) Donald, A. M.; Kramer, E. J.; Bubeck, R. A. The Entanglement Network and Craze Micromechanics in Glassy Polymers. *Journal of Polymer Science: Polymer Physics Edition* **1982**, 20 (7), 1129–1141. <https://doi.org/10.1002/pol.1982.180200703>.
- (36) Kramer, E. J. Microscopic and Molecular Fundamentals of Crazing. In *Crazing in Polymers*; Kausch, H. H., Ed.; Springer Berlin Heidelberg, 1983; pp 1–56.
- (37) Henkee, C. S.; Kramer, E. J. Crazing and Shear Deformation in Crosslinked Polystyrene. *Journal of Polymer Science: Polymer Physics Edition* **1984**, 22 (4), 721–737. <https://doi.org/10.1002/pol.1984.180220414>.
- (38) Kramer, E. J.; Berger, L. L. Fundamental Processes of Craze Growth and Fracture. In *Crazing in Polymers Vol. 2*; Kausch, H.-H., Ed.; Springer Berlin Heidelberg: Berlin, Heidelberg, 1990; Vol. 91/92, pp 1–68. <https://doi.org/10.1007/BFb0018018>.
- (39) Friedrich, K. Crazes and Shear Bands in Semi-Crystalline Thermoplastics. In *Crazing in Polymers*; Kausch, H. H., Ed.; Springer-Verlag: Berlin/Heidelberg, 1983; Vol. 52–53, pp 225–274. <https://doi.org/10.1007/BFb0024059>.
- (40) Argon, A. S.; Salama, M. M. Growth of Crazes in Glassy Polymers. *The Philosophical Magazine: A Journal of Theoretical Experimental and Applied Physics* **1977**, 36 (5), 1217–1234. <https://doi.org/10.1080/14786437708239790>.
- (41) Kambour, R. P. A Review of Crazing and Fracture in Thermoplastics. *Journal of Polymer Science: Macromolecular Reviews* **1973**, 7 (1), 1–154. <https://doi.org/10.1002/pol.1973.230070101>.
- (42) Taylor, G. I. The Instability of Liquid Surfaces When Accelerated in a Direction Perpendicular to Their Planes. I. *Proceedings of the Royal Society of London. Series A. Mathematical and Physical Sciences* **1950**, 201 (1065), 192–196. <https://doi.org/10.1098/rspa.1950.0052>.
- (43) Halary, J. L.; Laupretre, F.; Monnerie, L. *Polymer Materials: Macroscopic Properties and Molecular Interpretations*; Wiley, 2011.
- (44) Mills, P. J.; Kramer, E. J.; Brown, H. R. Real Time Small-Angle X-Ray Scattering from Polystyrene Crazes during Fatigue. *Journal of Materials Science* **1985**, 20 (12), 4413–4420. <https://doi.org/10.1007/BF00559330>.
- (45) Salomons, G. J.; Singh, M. A.; Bardouille, T.; Foran, W. A.; Capel, M. S. Small-Angle X-Ray Scattering Analysis of Craze-Fibril Structures. *Journal of Applied Crystallography* **1999**, 32 (1), 71–81. <https://doi.org/10.1107/S0021889898010486>.
- (46) Lode, U.; Pomper, T.; Karl, A.; von Krosigk, G.; Cunis, S.; Wilke, W.; Gehrke, R. Development of Crazes in Polycarbonate, Investigated by Ultra Small Angle X-Ray Scattering of Synchrotron Radiation. *Macromolecular Rapid Communications* **1998**, 19 (1), 35–39. [https://doi.org/10.1002/\(SICI\)1521-3927\(19980101\)19:1<35::AID-MARC35>3.0.CO;2-3](https://doi.org/10.1002/(SICI)1521-3927(19980101)19:1<35::AID-MARC35>3.0.CO;2-3).
- (47) Brown, H. R.; Sindoni, Y.; Kramer, E. J.; Mills, P. J. Diffraction Studies of Craze Structure. *Polymer Engineering and Science* **1984**, 24 (10), 825–832. <https://doi.org/10.1002/pen.760241013>.
- (48) Stoclet, G.; Lefebvre, J. M.; Séguéla, R.; Vanmansart, C. In-Situ SAXS Study of the Plastic Deformation Behavior of Polylactide upon Cold-Drawing. *Polymer* **2014**, 55 (7), 1817–1828. <https://doi.org/10.1016/j.polymer.2014.02.010>.

- (49) Mourglia-Seignobos, E.; Long, D. R.; Odoni, L.; Vanel, L.; Sotta, P.; Rochas, C. Physical Mechanisms of Fatigue in Neat Polyamide 6,6. *Macromolecules* **2014**, *47* (12), 3880–3894. <https://doi.org/10.1021/ma500256x>.
- (50) Djukic, S. Damage Mechanisms under Tensile Deformation of Amorphous and Low Semicrystalline Polymers. PhD Thesis, Université Lyon 1, 2020.
- (51) Preda, F. M. Dynamics of Polyamide in the Solid State in Presence of Solvents and in the Molten State. PhD Thesis, Université Lyon 1, 2016.
- (52) van Erp, T. B.; Govaert, L. E.; Peters, G. W. M. Mechanical Performance of Injection-Molded Poly(Propylene): Characterization and Modeling. *Macromolecular Materials and Engineering* **2013**, *298* (3), 348–358. <https://doi.org/10.1002/mame.201200116>.
- (53) Wu, S. *Polymer Interface and Adhesion*; M. Dekker New York, 1982; Vol. 188.
- (54) Jańczuk, B.; Wójcik, W.; Zdziennicka, A. Determination of the Components of the Surface Tension of Some Liquids from Interfacial Liquid-Liquid Tension Measurements. *Journal of Colloid and Interface Science* **1993**, *157* (2), 384–393. <https://doi.org/10.1006/jcis.1993.1200>.
- (55) Sorensen, C. M.; Oh, C.; Schmidt, P. W.; Rieker, T. P. Scaling Description of the Structure Factor of Fractal Soot Composites. *Phys. Rev. E* **1998**, *58* (4), 4666–4672. <https://doi.org/10.1103/PhysRevE.58.4666>.
- (56) Guinier, A.; Fournet, G. *Small Angle Scattering of X-Rays*, John Wiley and Son, New York.; 1955.
- (57) Beaucage, G.; Kammler, H. K.; Pratsinis, S. E. Particle Size Distributions from Small-Angle Scattering Using Global Scattering Functions. *Journal of Applied Crystallography* **2004**, *37* (4), 523–535. <https://doi.org/10.1107/S0021889804008969>.
- (58) Abramowitz, M.; Stegun, I. A.; Romer, R. H. Handbook of Mathematical Functions with Formulas, Graphs, and Mathematical Tables. *American Journal of Physics* **1988**, *56* (10), 958–958. <https://doi.org/10.1119/1.15378>.
- (59) Sztucki, M.; Narayanan, T. Development of an Ultra-Small-Angle X-Ray Scattering Instrument for Probing the Microstructure and the Dynamics of Soft Matter. *Journal of Applied Crystallography - J APPL CRYST* **2006**, *40*. <https://doi.org/10.1107/S0021889806045833>.
- (60) Charvet, A.; Vergelati, C.; Long, D. R. Mechanical and Ultimate Properties of Injection Molded Cellulose Acetate/Plasticizer Materials. *Carbohydrate Polymers* **2019**, *204*, 182–189. <https://doi.org/10.1016/j.carbpol.2018.10.013>.
- (61) Zafeiropoulos, N. E.; Davies, R. J.; Schneider, K.; Burghammer, M.; Riekel, C.; Stamm, M. The Relationship between Craze Structure and Molecular Weight in Polystyrene as Revealed by MSAXS Experiments. *Macromolecular Rapid Communications* **2006**, *27* (19), 1689–1694. <https://doi.org/10.1002/marc.200600453>.
- (62) Bridle, C.; Buckley, A.; Scanlan, J. Mechanical Anisotropy of Oriented Polymers. *Journal of Materials Science* **1968**, *3* (6), 622–628. <https://doi.org/10.1007/BF00757909>.
- (63) Landau, L. D.; Lifshitz, E. M. Chapter XV - Surfaces. In *Statistical Physics (Third Edition)*; Butterworth-Heinemann: Oxford, 1980; pp 517–537. <https://doi.org/10.1016/B978-0-08-057046-4.50022-1>.
- (64) Fisher, J. C. The Fracture of Liquids. *Journal of Applied Physics* **1948**, *19* (11), 1062–1067. <https://doi.org/10.1063/1.1698012>.
- (65) Roth, C.; Pye, J.; Baglay, R. Correlating Glass Transition and Physical Aging in Thin Polymer Films; 2016; pp 181–204. <https://doi.org/10.1201/9781315305158-8>.

- (66) Baglay, R. R.; Roth, C. B. Communication: Experimentally Determined Profile of Local Glass Transition Temperature across a Glassy-Rubbery Polymer Interface with a T_g Difference of 80 K. *The Journal of Chemical Physics* **2015**, *143* (11), 111101. <https://doi.org/10.1063/1.4931403>.
- (67) Baglay, R. R.; Roth, C. B. Local Glass Transition Temperature $T_g(z)$ of Polystyrene next to Different Polymers: Hard vs. Soft Confinement. *The Journal of Chemical Physics* **2017**, *146* (20), 203307. <https://doi.org/10.1063/1.4975168>.
- (68) Gabrielle, B.; Guy, L.; Albouy, P.-A.; Vanel, L.; Long, D. R.; Sotta, P. Effect of Tear Rotation on Ultimate Strength in Reinforced Natural Rubber. *Macromolecules* **2011**, *44* (17), 7006–7015. <https://doi.org/10.1021/ma2010926>.
- (69) Argon, A. A Theory for the Low-Temperature Plastic Deformation of Glassy Polymers. *Philosophical Magazine A-physics of Condensed Matter Structure Defects and Mechanical Properties - PHIL MAG A* **1973**, *28*, 839–865. <https://doi.org/10.1080/14786437308220987>.
- (70) Argon, A. S.; Hannoosh, J. G. Initiation of Crazes in Polystyrene. *The Philosophical Magazine: A Journal of Theoretical Experimental and Applied Physics* **1977**, *36* (5), 1195–1216. <https://doi.org/10.1080/14786437708239789>.
- (71) Argon, A. Craze Initiation in Glassy Polymers – Revisited. *Polymer* **2011**, *52*, 2319–2327. <https://doi.org/10.1016/j.polymer.2011.03.019>.
- (72) de Gennes, P. G. Wetting: Statics and Dynamics. *Rev. Mod. Phys.* **1985**, *57* (3), 827–863. <https://doi.org/10.1103/RevModPhys.57.827>.
- (73) Fields, R. J.; Ashby, M. F. Finger-like Crack Growth in Solids and Liquids. *Philosophical Magazine* **1976**, *33* (1), 33–48.
- (74) Donald, A. M. Crazing. In *The Physics of Glassy Polymers*; Haward, R. N., Young, R. J., Eds.; Springer Netherlands: Dordrecht, 1997; pp 295–341. https://doi.org/10.1007/978-94-011-5850-3_6.
- (75) Argon, A. S.; Bessonov, M. I. Plastic Flow in Glassy Polymers. *Polymer Engineering & Science* **1977**, *17* (3), 174–182. <https://doi.org/10.1002/pen.760170306>.
- (76) Hussein, N.; Long, D.; Fillot, L.-A.; Trouillet-Fonti, L. Aliphatic/Semi-Aromatic Block Copolyamide. US9688823B2, June 27, 2017.
- (77) Fillot, L.-A.; Jeol, S.; Long, D.; Hussein, N. Method for Increasing Fatigue Resistance of Polyamides. WO2014076139A1, May 22, 2014.